Circuit Mechanisms of Top-Down Attentional Control in a Thalamic Reticular Model

Qinglong L. Gu[1,*], Norman H. Lam[2,3,*], Michael M. Halassa[3,4], John D. Murray[1,2,†]

[1] *Department of Psychiatry, Yale University School of Medicine, New Haven, Connecticut, USA*
[2] *Department of Physics, Yale University, New Haven, Connecticut, USA*
[3] *Department of Brain and Cognitive Sciences, Massachusetts Institute of Technology, Cambridge, MA 02139, USA*
[4] *McGovern Institute for Brain Research, Massachusetts Institute of Technology, Cambridge, MA 02139, USA*
[*] *Equal contribution*
[†] *Correspondence: john.murray@yale.edu*

Summary

The thalamus is a key brain structure engaged in attentional functions, such as selectively amplifying task-relevant signals of one sensory modality while filtering distractors of another. To investigate computational mechanisms of attentional modulation, we developed a biophysically grounded thalamic reticular circuit model, comprising excitatory thalamocortical and inhibitory reticular neurons, which captures characteristic neurophysiological observations from the alert behaving animals. Top-down attentional control inputs onto reticular neurons effectively modulate thalamic gain and enhance downstream readout, to improve performance across detection, discrimination, and cross-modal task paradigms. Heterogeneity of thalamic responses plays an essential role in downstream decoding during attentional modulation. Dynamical systems analysis explains why reticular neurons are an especially potent site for top-down control, as implicated by experiments. Perturbation analysis reveals excitation-inhibition ratio as an effective parameter governing thalamic processing. These findings establish experimentally testable circuit mechanisms for attentional control in thalamus, with implications for distributed neural control of cognitive processing.

Keywords

Computational model; Thalamus; Thalamic reticular nucleus; Gain; Attention; Detection; Discrimination; Neural coding; Dynamical systems; Inhibition

Introduction

Selective attention is a core neurocognitive function involving flexible, context-dependent prioritization of information for perceptual and cognitive computations. In an environment with multiple stimuli or features, attentional modulation can enhance processing of selected sensory signals and filter out distractors in a goal-directed manner. For instance, selective attention can be flexibly deployed across sensory modalities, to attend to task-relevant stimuli of one modality (e.g., vision) while attenuating interference from another modality (e.g., audition) (Wimmer et al., 2015). A growing experimental literature shows that selective attention engages subcortical structures (Krauzlis et al., 2018), including the thalamus (Saalmann and Kastner, 2011; Halassa and Kastner, 2017). Within each thalamic nucleus, glutamatergic thalamocortical (TC) neurons process and transmit information to cortex for downstream computation. The thalamic reticular nucleus (TRN), which forms a thin capsule around thalamic nuclei, contains GABAergic reticular (RE) neurons which provide inhibition onto TC neurons (Jones, 2012). In an influential theoretical proposal, Crick (1984) hypothesized that selective attention could be implemented with the TRN acting as an attentional "spotlight," suggesting that "if the thalamus is the gateway to the cortex, the reticular complex might be described as the guardian of the gateway."

Studies in rodents, monkeys, and humans characterize sensory thalamus as a locus of attentional filtering under flexible top-down control via the TRN (O'Connor et al., 2002; McAlonan et al., 2008; Ahrens et al., 2015; Wimmer et al., 2015; Nakajima et al., 2019). For instance, Wimmer et al. (2015) recorded neuronal spiking activity from the visual TRN and lateral geniculate nucleus (LGN) in mice trained on a cross-modal attention task, in which a cue informed of the subject of which sensory modality (vision vs. audition) to base its behavioral response. TRN and LGN exhibited opposite modulations by attentional selection: when vision was the attended modality, visual TRN decreased firing activity and LGN exhibited increased activity and higher gain of stimulus response. Nakajima et al. (2019) found a pathway for this attentional control of thalamus, from the prefrontal cortex through the basal ganglia's inhibitory projections onto the TRN.

These convergent empirical findings raise key computational questions about the mechanisms and functions of attentional control in thalamic reticular circuits. At a mechanistic level, it is not known how top-down attentional control via the TRN, compared to direct projections to TC neurons, may differentially regulate thalamic processing. It is also unclear how such circuit mechanisms implement attentional modulation of bottom-up sensory signals and how downstream readout of thalamic activity can parse bottom-up from top-down signals. Computational modeling provides a useful framework for understanding how neural circuit mechanisms can subserve cognitive functions. Thalamic reticular dynamics such as oscillations have been modeled at the neuronal and microcircuit levels (Destexhe et al., 1993b; 1994; 1996; Wang et al., 1995; Bazhenov et al., 2000; Sohal et al., 2006). However, there has been relatively little biophysically grounded modeling of thalamic reticular circuits in dynamical regimes consistent with neural recordings from alert behaving animals, which could yield insight into the interplay of cellular and circuit mechanisms supporting attentional modulation.

To investigate these issues, we developed a biophysically grounded thalamic reticular circuit model and studied how modulation by top-down inputs can implement attentional control of stimulus processing. We found that this model, with circuit dynamics constrained by experiments to operate in the regime of alert behaving animals, can capture key experimentally observed phenomena of thalamic activity and its modulation by attention. Dynamical systems analysis explains why RE neurons are an especially potent site for top-down control, compared to TC neurons. The geometry of heterogeneous thalamic responses makes testable predictions for downstream readout of information from the confluence of bottom-up and top-down signals, for attentional enhancement of performance in detection, discrimination, and cross-modal task paradigms. Finally, sensitivity analysis reveals how dynamical and computational features depend on biophysical circuit properties. The model therefore provides theoretical insight into circuit mechanisms of attentional control, parsimoniously captures a range of experimental observations, and makes experimentally testable predictions for future studies of the thalamus's role in cognitive function.

Results

Thalamic Reticular Circuit Architecture

In this study we developed a thalamic reticular circuit model for selective attention which is parsimonious yet grounded in physiology and anatomy of the system (**Figure 1**; see **Methods**). The model consists of one population of excitatory thalamocortical (TC) neurons, and another of inhibitory reticular (RE) neurons. TC neurons receive stimulus inputs, from a particular modality, and TC outputs are considered to project to downstream areas for readout and processing. Various forms of top-down inputs, mediating modality-selective attentional control signals, may also target TC and RE neurons to modulate circuit responses. The TC and RE populations are coupled to each other through sparse synaptic connections, with projections from TC to RE mediated by excitatory AMPA receptors (AMPARs) and projections from RE to TC mediated by $GABA_A$ receptors (GABARs). Neither TC or RE neurons are synaptically coupled to other neurons of the same type (i.e., TC to TC, or RE to RE) (Jones, 2012; Hou et al., 2016). Each TC or RE population comprises 1000 spiking neurons, which are modeled as single-compartment Hodgkin-Huxley neurons with a minimal but sufficient set of membrane channels to implement characteristic features of TC and RE neurons, such as hyperpolarization-induced rebound burst spiking (Destexhe et al., 1993a; 1996; Wang and Buzsáki, 1996) (**Figure S1**).

Circuit Dynamics in Alert Awake State Regime

To enable modeling of thalamic reticular circuit dynamics during attentional control, we first constrained our circuit model to operate in a dynamical regime consistent with *in vivo* observations from alert behaving animals. Prior computational modeling studies of TC and RE neurons primarily focused on dynamics on neuronal dynamics observed *in vitro*, under anesthesia, or during sleep, in which TC and RE neurons can intrinsically generate strong oscillations between bursting and hyperpolarization (Wang et al., 1995; Destexhe et al., 1996; 1998; Bazhenov et al., 2002; Krishnan et al., 2016; Timofeev et al., 2020). In contrast, spontaneous activity in the alert awake state is characterized by irregular, quasi-asynchronous spiking with only intermittent bursting and lack of strong intrinsic oscillation (Bruno, 2006; Temereanca et al., 2008; Ramcharan et al., 2005; Hirai et al., 2017; Bastos et al., 2014; Saleem et al., 2017).

Synaptic parameters setting the strengths of TC-RE interconnections and background inputs could be constrained by characteristic neurophysiological observations, as follows. The quasi-asynchronous population firing rates and burst rates are set to be consistent with experimental findings (Ramcharan et al., 2005; Rodenkirch et al., 2019) (**Figures 2A–C**). How the circuit responds to perturbation can provide another useful empirical constraint. Halassa et al. (2011) found that a strong and brief optogenetic depolarization of RE neurons could evoked a transient response involving increased probability of TC bursting and an oscillatory bout in the spindle (7–15 Hz) frequency range. In our model, these evoked dynamics emerge through an interplay between cellular and circuit mechanisms (**Figures 2D–F**). Intrinsic cellular conductances drive hyperpolarization-induced rebound spiking (**Figures 2E**), and a damped oscillation in the spindle frequency arises through the reciprocal synaptic excitatory and inhibitory interactions between TC and RE neurons (**Figures 2F**). Spontaneous and evoked activity can thereby characterize the alert awake dynamical regime of a thalamic reticular circuit and constrain model parameters (**Figures 2G-I, S2**). Specifically, if synaptic connection strengths are too strong, the circuit will generate highly synchronous oscillations (**Figure S2A**), and if they are too weak, the circuit will not exhibit the spindle-like evoked activity in response to a transient RE drive (**Figure S2B**).

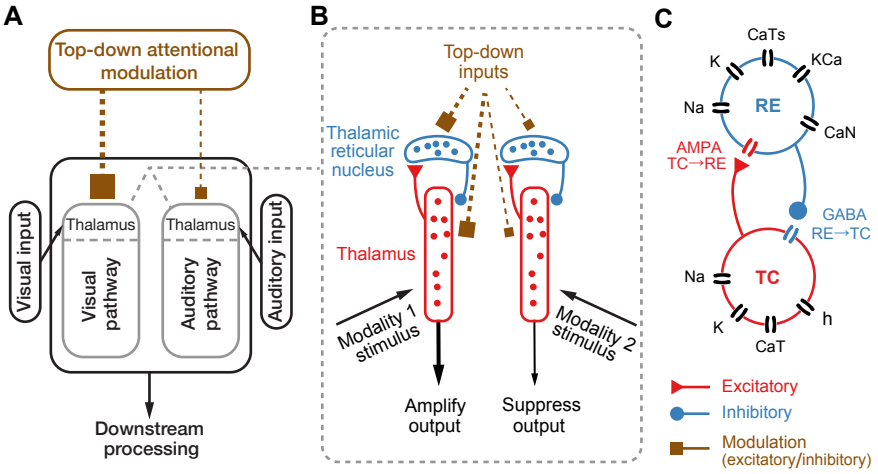

Figure 1: Model architecture for attentional control of thalamic reticular circuits. (A) Conceptual schematic of modality-selective attention. When receiving simultaneous stimulus inputs from multiple modalities (e.g., visual and auditory) for processing in downstream cortical areas, top-down inputs onto thalamic structures can mediate modality-selective attentional modulation of thalamic responses. **(B)** Thalamic circuit implementation of top-down modulation on selective attention. Distinct populations of excitatory thalamocortical neurons (TC, red) receive stimulus inputs from separate modalities and project their outputs to the cortex. Each population of TC neurons is reciprocally coupled to an associated population of inhibitory thalamic reticular neurons (RE, blue). To implement attentional control, top-down inputs to RE or TC neurons modulate thalamic outputs to the cortex, e.g., through amplification of stimulus signals from an attended sensory modality or suppression of those from a distractor modality. Top-down inputs can project to either TC or RE neurons, and can be either excitatory or inhibitory. **(C)** Single neuron models. Hudgkin-Huxley neurons with a minimal but sufficient set of characteristic channel conductances are used to simulate TC and RE neurons (see **Figure S1** and **Methods**). TC and RE populations are reciprocally connected through sparse synaptic projections, with excitatory connections from TC to RE mediated by AMPA receptors and inhibitory connections from RE to TC mediated by $GABA_A$ receptors.

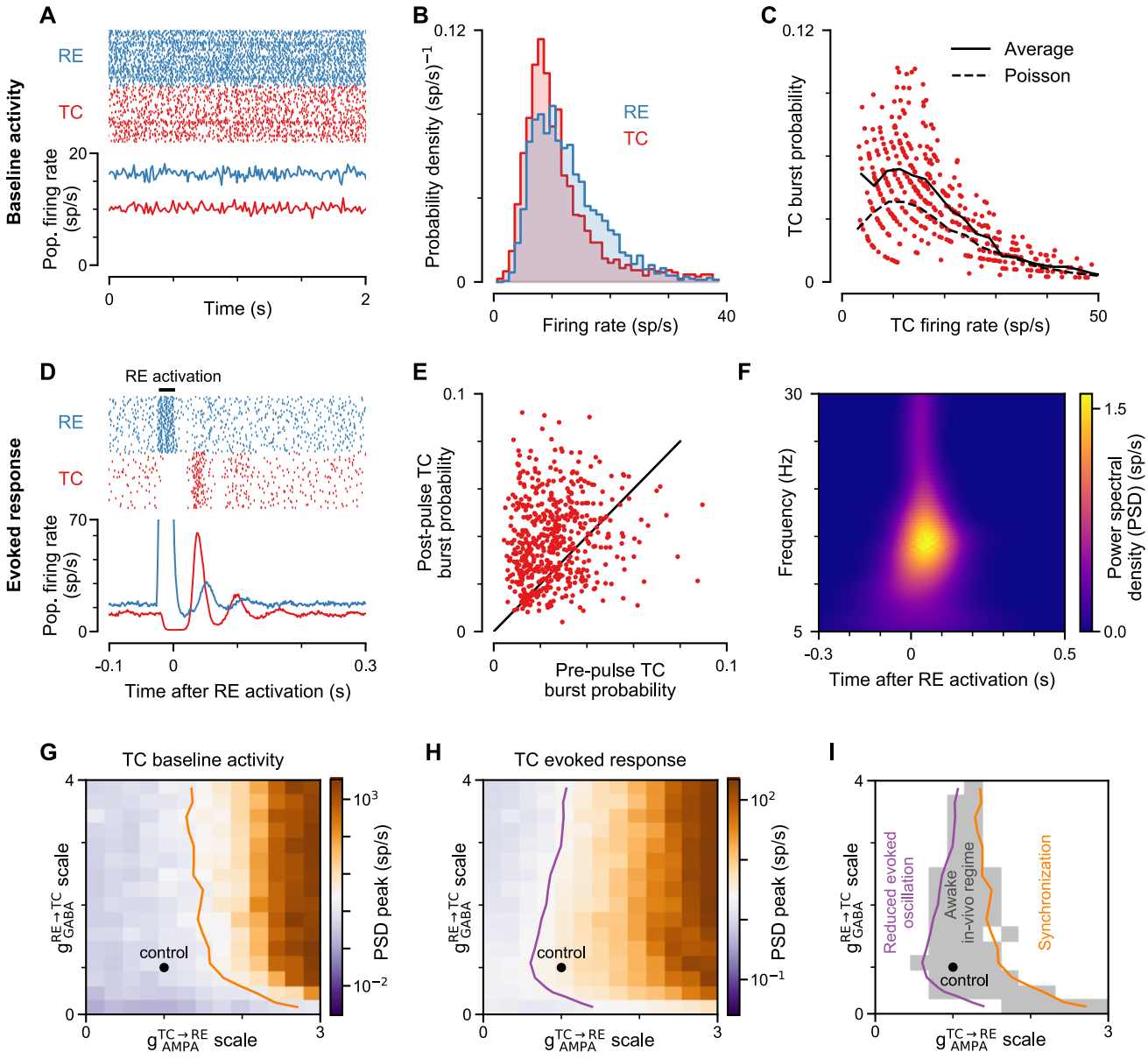

Figure 2: Thalamic reticular circuit model in alert awake regime. The circuit model is constrained to capture key circuit dynamics observed in alert behaving animals. **(A)** Rastergram showing quasi-asynchronous spiking activity in baseline state for RE (blue) and TC (red) neurons. **(B)** Distribution of TC and RE firing rates, which arises from heterogeneous recurrent and background connectivity. **(C)** Scatter plot of firing rate and burst probability across TC neurons. TC burst probability inversely correlates with its firing rate, and the average burst probability as a function of the firing rate (solid line) is higher than that of Poisson spike trains (dashed line). **(D)** Rastergram and evoked oscillation activity in response to pulse input to RE neurons. Black bar denotes time of pulse onset. **(E)** Burst probability post-pulse relative to pre-pulse. Burst probability is increased after RE pulse input. **(F)** Power spectral density (PSD) over time of evoked response to RE pulse. The evoked response demonstrates decaying oscillation in the spindle frequency. **(G)** Peak value of the PSD for spontaneous activity, as a function of $g_{\text{AMPA}}^{\text{TC}\to\text{RE}}$ and $g_{\text{GABA}}^{\text{RE}\to\text{TC}}$. Oscillation arises from strong coupling from TC to RE ($g_{\text{AMPA}}^{\text{TC}\to\text{RE}}$). Orange line denotes the upper bound where the circuit exhibits quasi-asynchronous spontaneous activity (see **Methods**). **(H)** PSD peak for the evoked response to RE pulse input as a function of $g_{\text{AMPA}}^{\text{TC}\to\text{RE}}$ and $g_{\text{GABA}}^{\text{RE}\to\text{TC}}$. Spindle oscillation is reduced with weak coupling from TC to RE ($g_{\text{AMPA}}^{\text{TC}\to\text{RE}}$) or strong coupling from RE to TC ($g_{\text{GABA}}^{\text{RE}\to\text{TC}}$). Purple line denotes the lower bound where the circuit exhibits an evoked spindle-like response consistent to experimental observations. **(I)** Parameter ranges of $g_{\text{AMPA}}^{\text{TC}\to\text{RE}}$ and $g_{\text{GABA}}^{\text{RE}\to\text{TC}}$ considered within the alert awake regime (shaded). Black dot denotes the control circuit.

Top-down Regulation of Thalamic Dynamics and Stimulus Processing

With the circuit model established and constrained by empirical observations, we investigated the effects of top-down control inputs and how they can implement attentional modulation of stimulus processing. We first consider our thalamic reticular circuit of one modality with top-down inputs taking the form of inhibition onto the RE neurons of the TRN, based on the basal ganglia pathway described by Nakajima et al. (2019) (**Figure 3A**). We found that increasing the strength of top-down drive suppresses RE firing rates, and elevates TC firing rates via disinhibition, which captures experimental observations when attention is directed toward the associated sensory modality (Wimmer et al., 2015; Nakajima et al., 2019) (**Figure 3B–D**). This pattern of opposite modulations for TC and RE reflects that the circuit does not operate in the inhibition-stabilized regime that is characteristic of cortical circuits (Ozeki et al., 2009; Litwin-Kumar et al., 2016; Sanzeni et al., 2020), due to the lack of recurrent excitatory TC-TC connections in thalamus.

In addition to its effects on baseline activity, top-down inhibition of RE also boosted the TC response to bottom-up stimulus inputs (**Figure 3C–E**). The TC response is a quasi-linear function of stimulus input amplitude, and strengthening the top-down input increases the gain of TC response (i.e., its slope as a function of stimulus amplitude). This increase in thalamic response gain by attention is also in line with experimental observations (Wimmer et al., 2015; Nakajima et al., 2019; McAlonan et al., 2008; O'Connor et al., 2002) (**Figure 3C–E**). Can this increase in TC response gain enhance downstream readout of the stimulus, for attentional improvement in behavior? To examine such questions, we built a decoder for stimulus detection, using the linear support vector machine (SVM) classifier framework, which is trained on the firing levels across the TC population (see **Methods**). We found that top-down modulation greatly improves detection accuracy through greater sensitivity (**Figure 3F**). These findings link top-down modulation of RE to increased TC response gain and improved downstream readout for psychophysical behavior.

Reticular vs. Thalamocortical Neurons as Sites for Top-Down Control

Are RE and TC populations similarly potent sites for thalamic regulation by top-down inputs? As an alternative to disinhibition of TC via RE neurons, which indirectly modulates TC response gain as shown above, top-down excitatory inputs (e.g., from cortex) could directly project to TC neurons to modulate their activity (Briggs and Usrey, 2008; Béhuret et al., 2015). We found that elevating top-down excitation to TC neurons can strongly increase the baseline firing rate of TC neurons (**Figure 4A-B**). RE neurons exhibited a weak increase in baseline firing rate, in contrast to the strong decrease induced by top-down inhibition to RE (**Figures 4B and 3B**). RE vs. TC as candidate sites for top-down input are therefore dissociable in their effects on baseline RE activity, and RE neurons as the primary site is consistent with experimental findings from Wimmer et al. (2015) and Nakajima et al. (2019).

Remarkably, top-down input to TC neurons exerted only a very weak effect on response gain, compared to top-down input to RE neurons (**Figures 4C** and **3E**). Top-down input to TC neurons had a correspondingly weak effect on detection accuracy from the downstream SVM decoder (**Figures 4D** and **3F**). Response gain and detection sensitivity increase monotonically with top-down modulation strength (**Figures 4E,F** and **S3**). Response gain and detection sensitivity were both much more potentially regulated by top-down input to RE neurons than top-down input to TC neurons (by factors of 6.8 and 3.6, respectively).

Dynamical Systems Analysis of Reduced Mean-Field Model

The above results reveal that RE neurons are more potent sites for top-down control of response gain, relative to TC neurons, with corresponding impact on downstream readout of stimulus signals. To understand the dynamical circuit

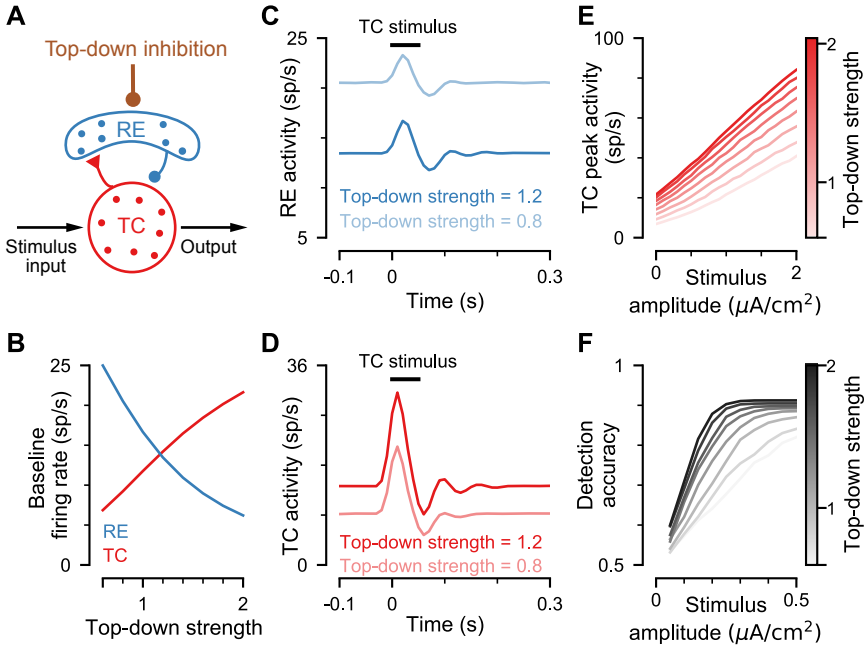

Figure 3: Top-down modulation via RE neurons can implement gain-like attentional control. (A) Circuit schematic. Top-down inhibition to RE neurons modulates the thalamic input-output response. **(B)** RE (blue) and TC (red) baseline firing rate as a function of top-down modulation strength. **(C, D)** RE and TC population activity in response to stimulus input with different top-down modulation strengths. **(E)** Circuit response function, i.e. TC firing rate as a function of stimulus strength, under different levels of top-down modulation strength. Darker color represents stronger top-down strength. **(F)** Detection accuracy of a downstream decoder, which is based on a linear support vector machine and operates on thalamic output firing rate patterns, under different levels of top-down modulation strength. Darker color represents stronger top-down strength.

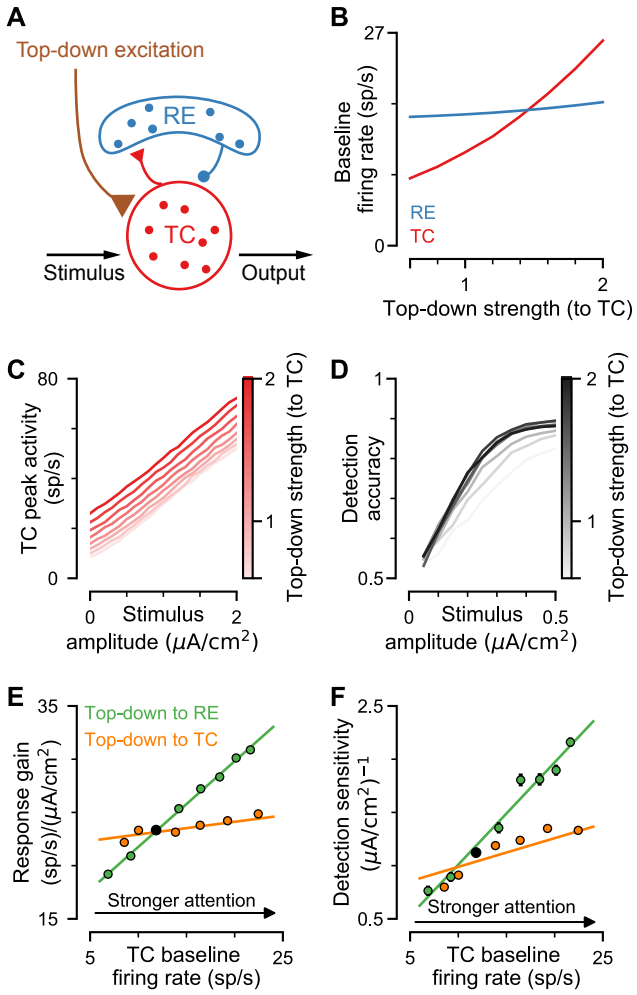

Figure 4: Top-down modulation via TC neurons, in contrast to via RE neurons. (A) Schematic of top-down excitation to TC neurons. **(B)** Baseline RE (blue) and TC (red) activity as a function of TC excitation. **(C)** Circuit response function, i.e. TC firing rate as a function of stimulus strength, under different levels of top-down excitation to the TC population. Darker colors represent stronger top-down excitation to TC neurons. **(D)** Detection accuracy of a downstream area to thalamic outputs under different levels of top-down modulation via TC neurons. Darker colors represent stronger top-down excitation to TC neurons. **(E)** Slope of the circuit response function, i.e. the response gain, as a function of top-down modulation strength, for inhibition to RE (green) or excitation to TC (orange). Response gain is derived from the TC response as a function of stimulus amplitude (from **Figures 4C** and **3E**). To facilitate comparison of RE vs. TC modulations, we parameterize the strength of top-down modulation in terms of its net effect on TC baseline firing rate (from **Figures 3B** and **4B**). **(F)** Sensitivity of detection accuracy as a function of top-down modulation strength. Sensitivity is defined as the slope of the initial part of the accuracy curve (from **Figures 3F** and **4D**). Top-down modulation through RE neurons has a larger effect than that through TC neurons. Black dot denotes the control circuit.

mechanisms underlying this differential sensitivity to RE vs. TC modulation, we developed and analyzed a reduced mean-field model of the thalamic reticular circuit. This reduced model comprises two dynamical variables representing the aggregate activity levels of the RE and and TC populations. The response gain of the circuit is an emergent property that is shaped by the interplay between the neuronal sensitivities and the feedback inhibition loop created by TC-RE interconnections (**Figure 5A**). Each neural population is governed by a neuronal transfer function describing the output firing rate as a function of the input current (commonly called an f-I curve), whose shape follows an expansive nonlinearity (**Figure 5B**). Neuronal and synaptic parameters were fit to, or derived from, the spiking circuit model (see **Methods**).

We found that the reduced mean-field model exhibits key properties of the spiking circuit, including that RE neurons are a more potent site for top-down regulation of response gain, compared to TC neurons (by a factor of nearly two, **Figure 5C**). The steady-state TC and RE activity levels under specific inputs into the circuit. As in the spiking circuit, top-down input via TC vs. RE neurons produces dissociable changes in the firing rates of RE neurons, which reflects the non-inhibition-stabilized regime (Ozeki et al., 2009; Litwin-Kumar et al., 2016) (**Figure 5D**). The analytical tractability of the reduced model allows calculation of the circuit response gain as a function of TC and RE activity levels. Top-down input onto RE, compared to TC, shifts the circuit to a state of higher response gain (**Figure 5E**). The mechanistic basis of this difference is revealed by the analytical expression for response gain (**Equation 16** in **Methods**) with dependence on the RE and TC neuronal sensitivities, i.e., the slopes of the neuronal input-output transfer functions (**Figure 5B**): response gain increases with higher TC neuronal sensitivity (and firing rate), and decreases with higher RE neuronal sensitivity (and firing rate). TC neuronal sensitivity is increased by top-down input to RE or to TC (**Figure 5F**). With top-down inhibition to RE, RE neuronal sensitivity decreases (**Figure 5G** left), which in turn boosts response gain. In contrast, with top-down excitation to TC, RE neuronal sensitivity increases (**Figure 5G** right), which in turn lowers response gain and counteracts the contribution from TC sensitivity. These analyses thereby give insight into how the interplay of neuronal and circuit properties give rise to the differential potency of RE as a site for top-down control of thalamic gain.

Downstream Decoding via Heterogeneous Population Activity

As shown above in the spiking circuit, top-down modulation via RE neurons improves performance of a downstream decoder trained for stimulus detection (**Figures 3F, 4F**). We next investigated the population coding principles by which downstream readout can be facilitated by top-down modulation of distributed TC response patterns. The decoder we implemented is a linear support vector machine (SVM) trained on the patterns of firing-rate activity across the heterogeneous population of 1000 TC neurons (**Figure 6A**) (see **Methods**). The population-activity decoder can be viewed geometrically as a classifier hyperplane in the high-dimensional space of neuronal activity (**Figure 6B**). To examine whether a distributed code across heterogeneous neurons is important for decoding, we also considered a second decoder whose input is only the mean firing rate averaged across the TC population.

We first varied the top-down strength and characterized its impact on different types of errors in the detection task. From signal detection theory, decoder errors can be decomposed in false alarms (i.e., responding 'yes' when the stimulus was absent) and misses (i.e., responding 'no' when the stimulus was present) (**Figure S4A**). The decoder based on population-averaged activity exhibited a sharp tradeoff between misses and false alarms as attentional strength varied (**Figure 6D**), in a manner consistent to classic signal detection theory. This tradeoff arises in the population-averaged decoder because stimulus input and top-down modulation both increase population averaged activity (**Figure 6E**). Remarkably, we found that strengthening top-down modulation reduced both types of errors for the decoder based on heterogeneous population activity patterns (**Figure 6C**). Under stronger top-down modulation, TC baseline activity is elevated yet there is decreased probability of downstream misclassification of that activity pattern as stimulus presence. These findings show that the improvement in downstream readout due to modulation of a distributed code across TC neurons, rather than their aggregate activity level.

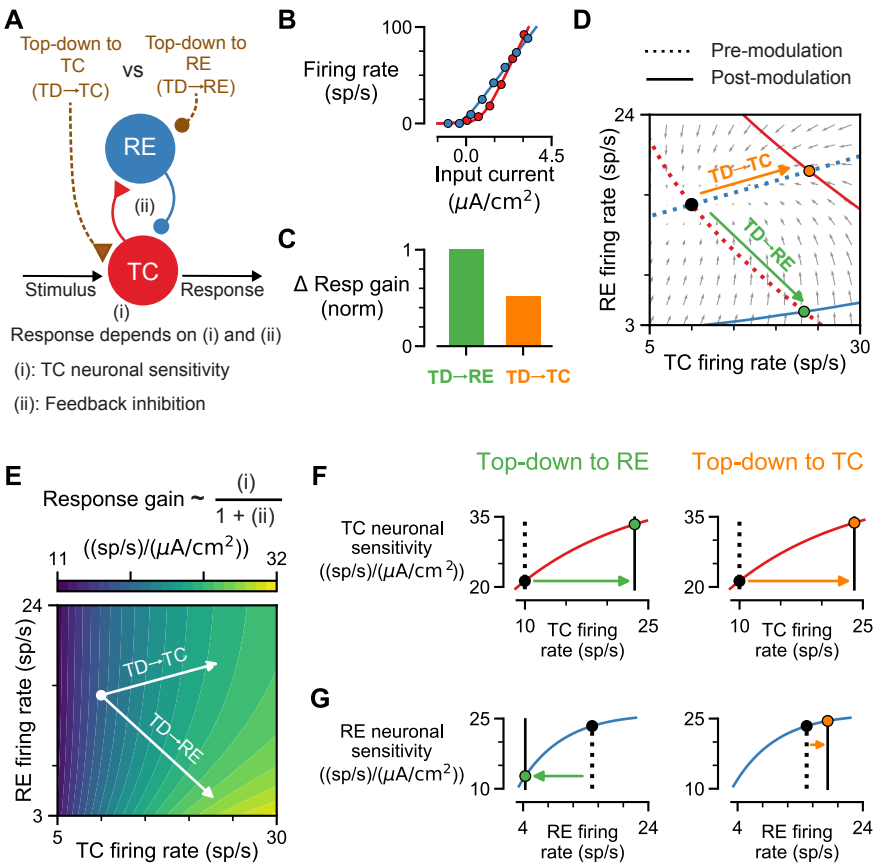

Figure 5: Mean-field analysis of gain control by top-down inputs. (A) Schematic of mean-field firing-rate circuit model, with TC (red) and RE (blue) activity as two dynamical variables. Top-down (TD) inhibition and excitation (brown) modulate the circuit through RE (TD→RE) and TC (TD→TC) populations, respectively. **(B)** Neuronal transfer function (f-I curve) of the RE and TC populations. Parameters of the functions (red and blue lines) were fit to simulated spiking data from the TC and RE single-neuron models (red and blue dots). **(C)** The effects of TD→RE and TD→TC modulation on the circuit response gain. TD→RE vs. TD→TC pathways are compared by setting top-down strengths such that they have the same elevation of TC baseline firing rate (as shown in **D**). For ease of comparison, changes in response gain are normalized by that induced by TD→RE. Top-down modulation via RE increases response gain more than via TC. **(D)** Phase-plane analysis showing nullclines of TC (red) and RE (blue) firing rates, with solid lines representing nullclines under top-down modulation. Intersections of the nullclines are the steady-state fixed points of the circuit (black for control; orange and green for states under top-down modulation via TC and RE, respectively). The small grey arrows represent the vector field for activity flow in the control state. **(E)** Circuit response gain as a function of TC and RE firing rates. The solid and dashed arrows denote the direction of the RE and TC modulation effect, respectively. **(F)** TC neuronal sensitivity, i.e. the slope of the TC neuronal transfer function, as a function of TC firing rate under top-down modulation via RE (left) or TC (right). Both top-down modulations can increase TC activity and its neuronal sensitivity at the similar level. **(G)** RE neuronal sensitivity as a function of its firing rate under top-down inputs to RE (left) or TC (right). Top-down modulation via RE decreases RE firing rate (left) whereas top-down modulation via TC increases RE firing rate (right), resulting in distinct gain effects by the two modulations (as shown in **Figure 4E**). The top-down inputs drive the circuit state from the black dot to the colored dots.

To gain further insight into the neural coding principles for attentional enhancement of performance, we examined geometric relationships of coding axes in the high-dimensional space of TC activity patterns (**Figures 6F–H, S4, S5**). The weight vector of the SVM decoder defines an axis in activity space, perpendicular to the classifier hyperplane, that assigns a score to each activity pattern by its projection along the decoder axis. In addition, we used regression analysis to define other weight vectors related to three aspects of TC activity: (i) bottom-up, reflecting the stimulus; (ii) top-down, reflecting the influence of the attention signal itself; and (iii) the interaction of bottom-up and top-down, reflecting attentional gain-like modulation of stimulus representations.

As expected, the bottom-up weight vector has a positive projection onto the decoder axis, so that stronger stimuli increase decoder scores (**Figure 6F–H**). Interestingly, the top-down weight vector has a weak negative projection onto decoder axis. In the absence of bottom-up stimulus, stronger top-down modulation thereby yields stronger negative decoder scores, which reduces false alarms. Finally, the bottom-up–top-down interaction weight vector has a strong positive projection onto the decoder axis. Gain-like modulation by top-down signals thereby increases decoder scores during stimulus presentation, which reduces misses. These functional analyses reveal how top-down modulation can increase the separability of TC activity patterns for stimulus on vs. off conditions to improve behavioral performance. These geometric properties also provide predictions for analysis of empirical TC spiking activity during attentional tasks.

Top-Down Modulation of Discrimination Performance

The analyses above used decoders trained in a detection task paradigm, to classify stimulus presence from absence. A second canonical task paradigm is categorical discrimination, wherein the subject must distinguish which of two stimuli is presented. To study this paradigm, we introduced two stimulus patterns as inputs to the circuit, defined as two Gaussian-tuned inputs which partially overlap in their projections onto TC neurons (**Figure 7A**). Note that top-down projections onto the RE population here is non-specific and unstructured, and therefore is not informed by the stimuli or discrimination boundary. To characterize the impact of top-down attentional modulation on downstream readout we trained a linear SVM decoder to classify which stimulus was presented (see **Methods**). Overall, we found that top-down modulation has a similar effect on discrimination as on detection. Specifically, top-down modulation via RE can improve discrimination performance (**Figures 7B**). Modulation via RE was more effective, compared to TC, at enhancing discrimination sensitivity (**Figures 7C**). The generated weight vectors for bottom-up stimulus and bottom-up–top-down interaction correlate with the SVM weight vector, with opposite signs for the two input identities (**Figure 7D**, also see **Figure S6**).

Attentional Filtering of Distractors to Prevent Interference

We next considered the important attentional function of flexibly regulating stimulus processing across multiple sensory modalities according to task demands. Experimental studies have characterized contextual control of thalamic processing in tasks with sensory selection from cross-modal stimuli (Wimmer et al., 2015; Ahrens et al., 2015; Nakajima and Halassa, 2017). In this task paradigm, a contextual cue first indicates which sensory modality should be attended as a target, and the other modality should be ignored as a distractor. Stimuli are presented simultaneously in both modalities, and behavioral response should be based on the specific stimulus in the attended modality.

In our model, the stimulus from each modality is sent to a separate TC-RE circuit (i.e., signals for two modalities enter separate thalamic nuclei and associated TRN regions) (**Figure 7E**). To apply attentional control, RE neurons for the attended modality will be strongly inhibited by top-down input, while RE neurons for the unattended modality will be only weakly inhibited. This allows the signal from the attended modality to be amplified, and that from the unattended modality

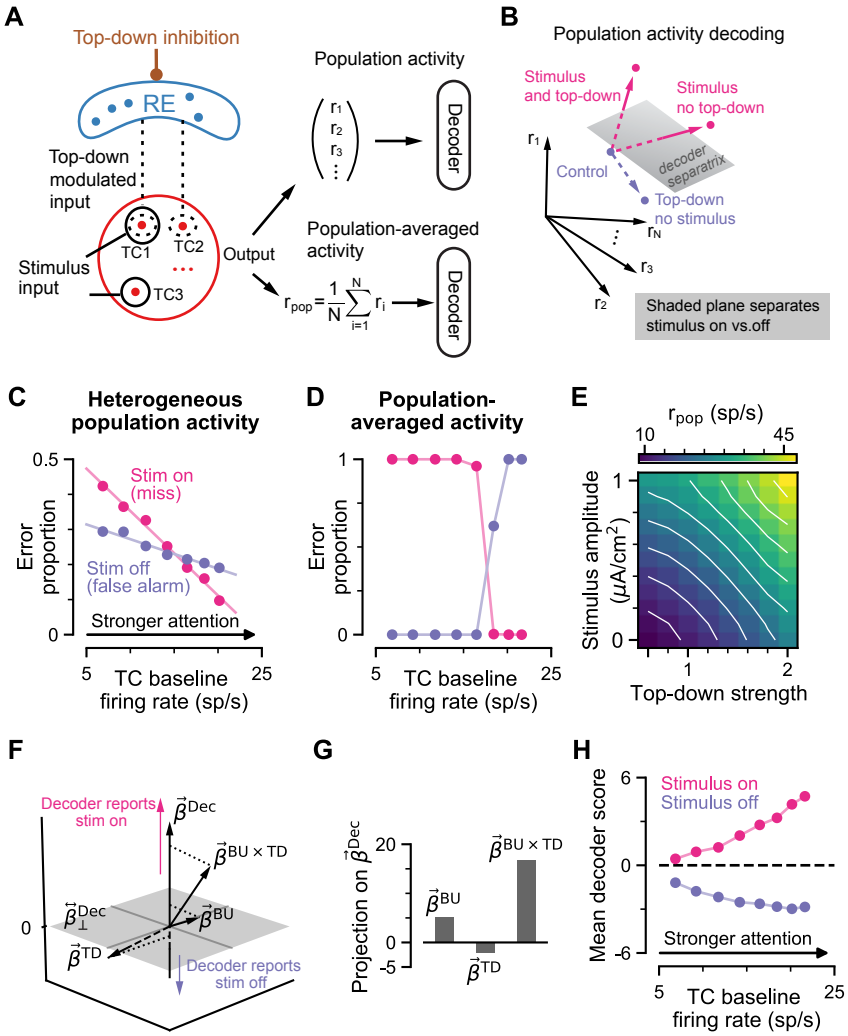

Figure 6: Downstream decoding utilizes heterogeneous population activity patterns for detection. (A) Schematic of readout via population decoders. Heterogeneity of circuit properties leads TC neurons to differ in their net inputs from bottom-up stimulus and top-down (mediated by RE) pathways. TC output can be decoded via high-dimensional patterns of population activity (top) or alternatively via the mean activity averaged across the TC population (bottom) (r_{pop}). Here the decoders are implemented as linear support vector machines (SVMs). **(B)** Schematic of population-activity decoding in the detection paradigm. The SVM decoder corresponds to a hyperplane separatrix that maps activity patterns on each side of the hyperplane to "stimulus on" vs. "stimulus off" reports. **(C)** For the heterogeneous population activity decoder, top-down modulation via RE improves detection performance by reducing error rates for both misses and false alarms. Misses (pink) vs. false alarms (purple) are error types when the stimulus was on vs. off, respectively. TC baseline activity serves as a proxy for top-down modulation via RE. **(D)** The population-averaged activity decoder exhibits a trade-off between miss and false alarm rates, as top-down strength is varied. **(E)** The population firing rate (r_{pop}) as a function of bottom-up stimulus amplitude and top-down strength. Both factors increase the mean population firing rate in a similar manner, explaining the poor performance of the population-averaged decoder. **(F)** Geometric relationships among coding and decoding axes in the TC activity space. Shown are regression weight vectors of the bottom-up stimulus ($\vec{\beta}^{\text{BU}}$), top-down modulation ($\vec{\beta}^{\text{TD}}$), and their interaction ($\vec{\beta}^{\text{BU}\times\text{TD}}$), in the 3-dimensional subspace spanned by $\vec{\beta}^{\text{BU}}$, and $\vec{\beta}^{\text{TD}}$, and the weight vector of the SVM decoder $\vec{\beta}^{\text{Dec}}$ (see **Methods**). **(G)** Projections of $\vec{\beta}^{\text{BU}}$, $\vec{\beta}^{\text{TD}}$ and $\vec{\beta}^{\text{BU}\times\text{TD}}$ onto $\vec{\beta}^{\text{Dec}}$. $\vec{\beta}^{\text{Dec}}$ has a positive alignment with $\vec{\beta}^{\text{BU}}$ and $\vec{\beta}^{\text{BU}\times\text{TD}}$, and a weak negative alignment with $\vec{\beta}^{\text{TD}}$. Top-down modulation via RE improves detection performance mainly through gain modulation, evident from the strong positive alignment of $\vec{\beta}^{\text{Dec}}$ with $\vec{\beta}^{\text{BU}\times\text{TD}}$. **(H)** The average SVM score (i.e. the projection of the circuit activity onto $\vec{\beta}^{\text{Dec}}$), as a function of top-down modulation via RE, when the stimulus is present (pink) or absent (purple). Top-down modulation shifts both away from the classifier boundary at 0, leading to reduced rates of misses and false alarms as shown in **(C)**.

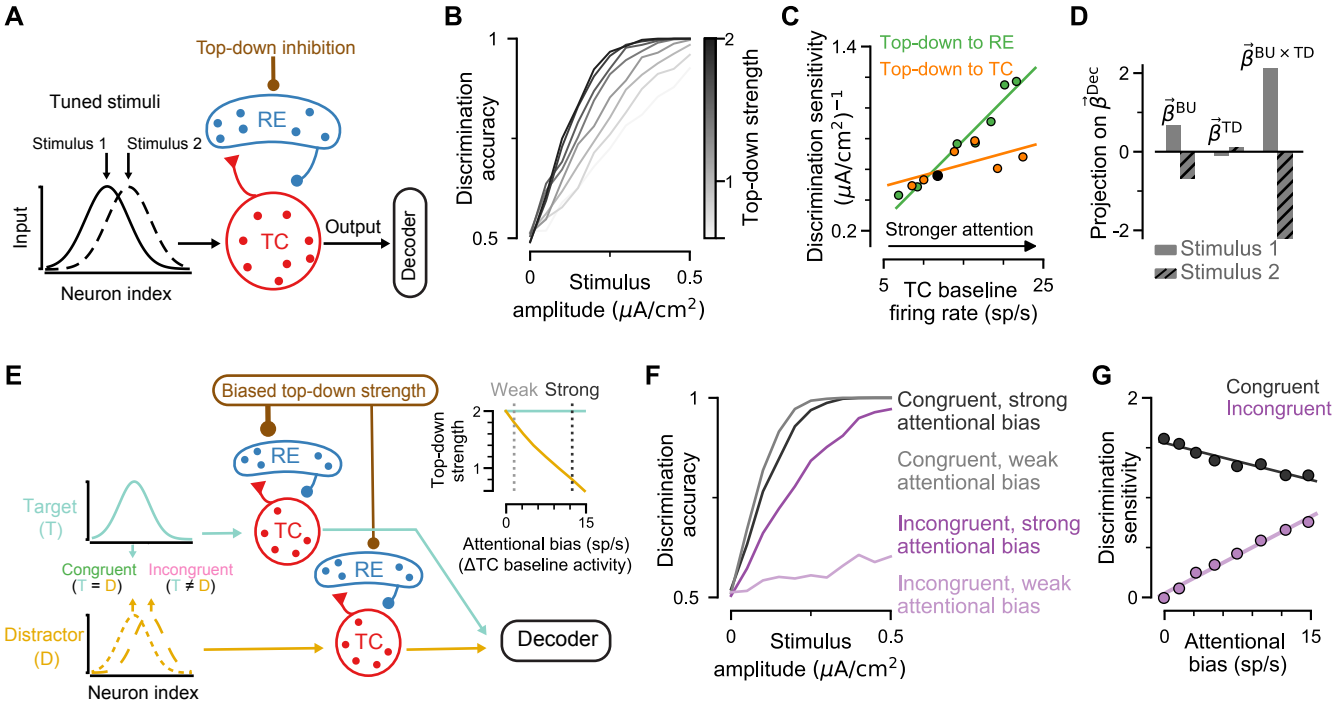

Figure 7: Attentional control of discrimination performance. (A) Schematic of uni-modal discrimination paradigm. Two tuned, partially overlapping stimulus patterns are used as inputs to the TC population. On each trial, one stimulus is presented, with variable amplitude to control difficulty. A downstream decoder is trained on TC output to classify which stimulus was presented. Top-down modulation is via non-specific inhibition to RE. **(B)** Discrimination accuracy of a downstream decoder under different levels of top-down modulation strength. Darker colors represent stronger top-down modulation. **(C)** Discrimination sensitivity of discrimination accuracy as top-down strength is varied, for modulation via RE vs. via TC. **(D)** Projections of the bottom-up stimulus, top-down modulation, and interaction weight vectors onto the SVM-based decoder axis, for each of the two stimuli (grey and hashed). Similar to the findings for detection (**Figure 6E**), the different sign of each projection weight indicates that top-down modulation via RE can increase the performance on the discrimination task through the gain-like interaction of bottom-up and top-down signals ($\vec{\beta}^{\mathrm{BU}\times\mathrm{TD}}$). **(E)** Schematic of the cross-modal (e.g., visual and auditory) discrimination paradigm. Here there are two TC-RE circuits, each corresponding to a different modality. Biased top-down modulation via RE across modalities allows attention toward the target modality (cyan) and filtering of the distractor modality (yellow), as well as contextual switching of which modality is target vs. distractor. The target and distractor stimuli can be either congruent, such that they map to the same readout response, or incongruent, such that they provide contrasting information. (Inset) Top-down strengths target and distractor modalities as a function of the attentional bias. The attentional bias is defined as the difference between the TC baseline activity in the attended modality to that in unattended modality (i.e., ΔTC baseline activity). **(F)** Discrimination accuracy of a downstream decoder, for congruent (black) and incongruent (purple) trials with strong (dark) and weak (light) attentional bias. **(G)** Discrimination sensitivity as a function of attentional bias, for congruent and incongruent trials. Attentional bias can enhance discrimination accuracy for incongruent trials by filtering out distractor stimuli. Across all conditions, the top-down modulatory input into the attended modality is held constant.

to be suppressed. Here we controlled the attentional bias by parametrically varying the top-down strength to the distractor modality. Importantly, the stimuli from the two modalities can be congruent, such that both stimuli consistent in their mapping to a response, or they can be incongruent, such that the two stimuli map to opposing responses (Ahrens et al., 2015).

We found that in the cross-modal paradigm, the circuit model demonstrates higher discrimination accuracy for congruent trials than for incongruent trials (**Figure 7F,G**). Strong attentional bias dramatically improves performance on incongruent trials, because the distractor stimulus signal is suppressed and filtered out relative to the target signal. This filtering also attenuates the performance benefit from the distractor in congruent trials. Attentional bias results in a performance tradeoff, although congruent trials still have higher sensitivity than incongruent trials and the net effect of attentional bias in improved performance. These findings suggest top-down modulation can implement flexible cross-modal filtering out of irrelevant signals to prevent interference with contextual behavior based on attended signals.

Sensitivity Analysis of Biophysical Perturbations

An important advantage of a biophysically grounded circuit model is that we can analyze how emergent dynamics and computations are shaped by neuronal and synaptic elements at the level of channel conductances. We approached this from the perspective of a sensitivity analysis, measuring how strongly a feature is changed by a small perturbation of a given parameter. Sensitivity analysis can reveal along which axes in parameter space the circuit features are sensitive or robust, and how different parameters could trade off or compensate for perturbations. Furthermore, it can reveal which features are sensitive or robust to perturbation, and how features covary with each other under perturbation.

We perturbed 6 biophysical parameters (4 synaptic and 2 cellular) (**Figure 8A**), and measured 7 features (3 dynamical and 4 task-computational), generating a feature sensitivity matrix (**Figure 8B**). We found that the features sensitivities varies greatly across features and parameters. Averaging across all features, the RE-specific parameters generated greater feature sensitivities than did TC-specific or synaptic parameters (**Figure 8B** top). This finding is consistent with the conclusion that RE neurons are a potent site for modulation of thalamic processing, as well as with proposals that RE neurons may be a site of vulnerability.

To gain further insight, we analyzed the feature sensitivity matrix using singular vector decomposition (SVD) (which is essentially principal component analysis but without mean subtraction; see **Methods**). The singular vectors from SVD associated with the top k singular values define the closest approximation to the feature sensitivity matrix by a rank-k matrix. One way to view SVD is consider each of the six perturbations as a point in the seven-dimensional space of features. The leading singular vector, SV1, defines the axis in feature space that best approximates the set of perturbation points. We found that SV1 explains 85% of the power in feature sensitivity, which indicates that the circuit's sensitivity to perturbations is approximately one-dimensional (**Figure 8C**). We found that the weights of SV1 are all the same sign, indicating that all features increase or decrease together along this axis (**Figure 8B** right, **Figure S7**). Finally, we examined the SV1 scores of the perturbation points, i.e. their projection along the SV1 axis. TC- and RE-related perturbations have opposite-sign scores, with synaptic perturbations at intermediate scores. We can therefore characterize the dominant mode of sensitivity as capturing alteration in excitation-inhibition balance.

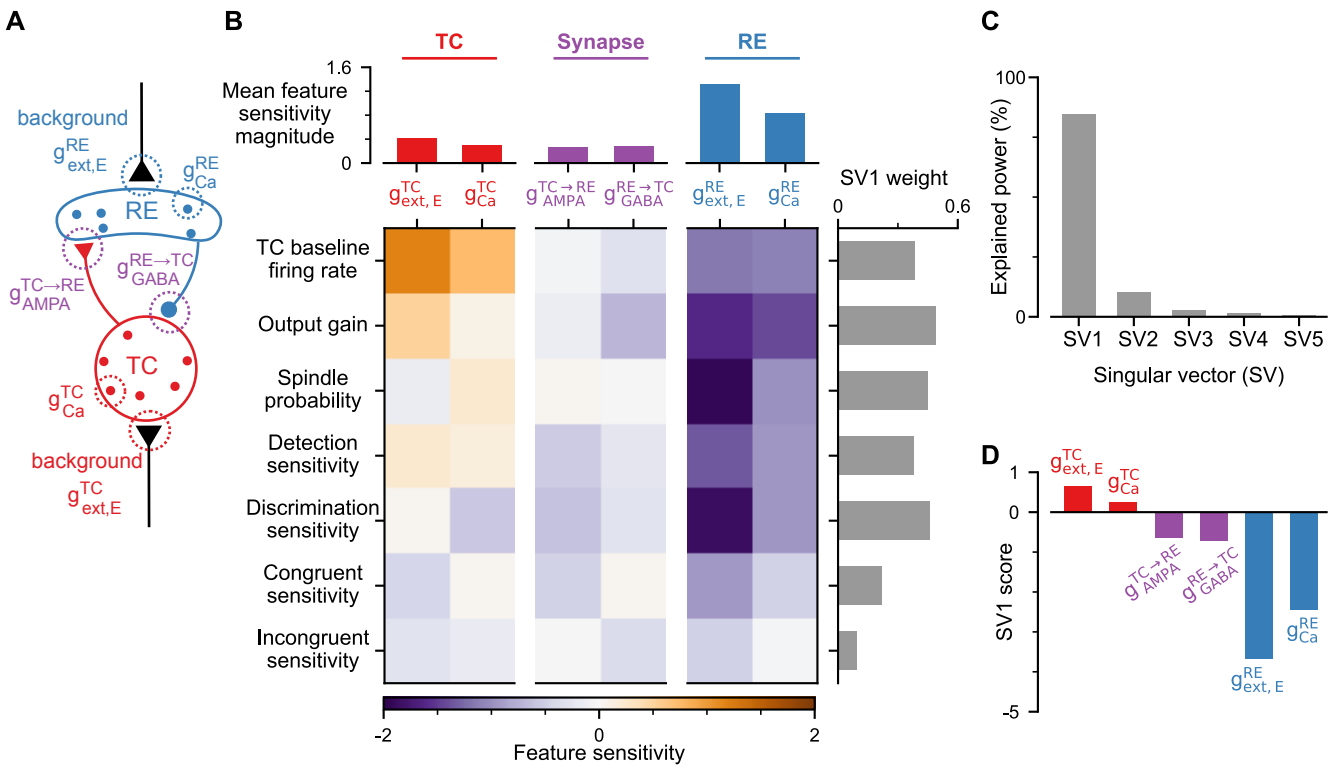

Figure 8: Sensitivity analysis of circuit dynamics and computations. **(A)** Schematic of biophysical parameters subject to perturbation, related to TC (red), RE (blue), and synaptic (purple) properties. Parameters were background excitatory AMPA conductances ($g^{\text{TC}}_{\text{ext,E}}$ and $g^{\text{RE}}_{\text{ext,E}}$), cellular calcium conductances ($g^{\text{TC}}_{\text{Ca}}$ and $g^{\text{RE}}_{\text{Ca}}$), and the synaptic connections between TC and RE populations ($g^{\text{TC}\to\text{RE}}_{\text{AMPA}}$ and $g^{\text{RE}\to\text{TC}}_{\text{GABA}}$). **(B)** (Bottom) Sensitivity value of seven dynamical and computational features to various perturbations. Feature selectivity is defined as the ratio of the proportional change in the feature to the proportional change in the parameter. A feature sensitivity of 1 means a 1% perturbation would drive a 1% change in the feature. (Top) Mean feature sensitivity amplitude across features for each perturbation. RE perturbations are especially potent. (Right) Weights of the first singular vector (SV1) of the feature selectivity matrix, in terms of the feature components, derived from singular value decomposition (SVD). SV1 is the axis in feature space that maximally captures the patterns of feature alterations across perturbations (see **Methods**). **(C)** Explained power of the leading singular vectors. SV1 explains 85% of the power in feature sensitivity matrix across perturbations, revealing a quasi-one-dimensional effect of biophysical perturbations on the set of features. **(D)** SV1 scores of the perturbations (i.e. projections of the perturbation vector along SV1). TC perturbations vs. RE perturbations are separated, revealing the quasi-one-dimensional dependence of the circuit on perturbation to excitation-inhibition balance.

Discussion

In this study, we developed a biophysically grounded, yet parsimonious, model of a thalamic reticular circuit, which is constrained by experimental findings to operate in the dynamical regime observed in alert behaving animals. The circuit model captures a number of key experimentally observed phenomena related to the thalamus and attention, including gain-like modulation of responses controlled by top-down control signals. Attentional modulation resulted in improved performance for downstream readout in detection, discrimination, and cross-modal task paradigms, with heterogeneity of thalamic response being critical for downstream decoding. Dynamical systems analysis reveals mechanisms by which the inhibitory TRN acts a preferentially potent site for attentional control. Finally, sensitivity analysis revealed excitation-inhibition ratio as a key effective parameter governing thalamic activity and attentional modulation.

Gain modulation of neuronal responses can be found across cortical and subcortical brain areas and is associated with various cognitive functions including attention (Ferguson and Cardin, 2020). In different circuits, gain control may be mediated by mechanisms such as synaptic noise (Ly and Doiron, 2009), active dentrites (Mehaffey, 2005) and diversity of interneuron populations (Litwin-Kumar et al., 2016). That the thalamic gain is more potently regulated by top-down modulation of RE neurons in the TRN, compared to direct modulation of TC neurons, is a key finding from our model. Interestingly, disinhibitory motifs are also prominent in neocortical microcircuits, and this computational principle may support contextual modulation of cortical state and response gain (Kepecs and Fishell, 2014; Fu et al., 2014; Litwin-Kumar et al., 2016; Yang et al., 2016). This circuit motif, of TRN mediating top-down control of thalamic processing, is supported by experimental studies. In particular, Wimmer et al. (2015) found that prefrontal-dependent sensory selection decreased baseline activity in TRN and increased it in thalamus, which in our model is consistent with top-down modulation via RE but not via TC. Nakajima et al. (2019) found convergent evidence that the attentional control of thalamic processing by prefrontal cortex was mediated through a basal ganglia pathway, which provides GABAergic inhibitory input to TRN from the globus pallidus. Basal ganglia-mediated inhibition of RE neurons thereby suppresses their activity and disinhibits TC neurons, which our model suggests increases TC response gain more effectively than would direct glutamatergic input to TC neurons.

Heterogeneity of thalamic activity patterns plays a critical role for attentional modulation to enhance downstream readout of stimulus information. Because both bottom-up and top-down inputs increase TC mean firing rates, readout of aggregate activity cannot disambiguate stimulus from attention signals. In the heterogeneous spiking circuit model, TC neurons are differentially responsive to bottom-up stimulus, top-down modulation, and their gain-like interaction, which allows downstream readout to harness attentional gain modulation to improve performance in detection and discrimination paradigms. These features could not be captured in homogeneous or mean-field models of thalamus (Roberts and Robinson, 2012; Jaramillo et al., 2019). Importantly, model predictions for geometrical relationships of TC coding axes can be tested in future analyses of spike-train recordings from thalamus during tasks that manipulate stimuli and attentional states (Wimmer et al., 2015; Nakajima et al., 2019).

The circuit model developed here is parsimonious, including key biophysical elements, and provides opportunities for extension to address additional neurobiological questions in future computational studies. For instance, models can be extended to incorporate the rich diversity of short-term synaptic plasticity dynamics at their inputs and local synaptic connections (Sherman, 2012; Usrey et al., 1998; Crandall et al., 2015). Furthermore, the TRN contains subcircuits involving distinct inhibitory cell types with different neuronal and synaptic properties (Ahrens et al., 2015; Clemente-Perez et al., 2017; Li et al., 2020; Martinez-Garcia et al., 2020). The model can also be extended to study regional specialization of TC-RE microcircuitry. Both TC and RE neurons exhibit specialization in their neuronal and synaptic properties across thalamus, following a hierarchical organization from primary sensory to higher-order regions (Phillips et al., 2019; Wei et al., 2011; Li et al., 2020; Martinez-Garcia et al., 2020). For instance, there is evidence that higher-order TC neurons are more intrinsically bursty than sensory TC neurons (Wei et al., 2011; Ramcharan et al., 2005). Thalamic burst firing can

profoundly shape information transmission and may be under top-down control (Wolfart et al., 2005; Whitmire et al., 2016; Alitto et al., 2019; Aizenberg et al., 2019) (**Figure S8**). Therefore, modeling circuit parameters which covary according to a hierarchical organization, from sensory to higher-order thalamic nuclei, could enable investigation into dynamical and computational specialization of thalamic reticular circuits.

In the present model, synaptic connectivity between TC and RE neurons is unstructured, random and sparse. There remain open questions about whether TC-RE connectivity forms a "closed-loop" motif, in which RE neurons inhibit the same TC neurons that excite them, or an "open-loop" motif in which RE neurons instead project to other TC neurons than those than excite them (Pinault, 2004; Halassa and Acsády, 2016). A closed-loop motif can implement feedback inhibition, whereas an open-loop motif can implement lateral inhibition. TRN-mediated lateral inhibition in thalamus could potentially operate at multiple scales, such as tuned lateral inhibition or normalization within a thalamic nucleus or cross-modal competition between nuclei. TRN neurons exhibit selectivity to bottom-up stimulus features (Hirsch et al., 2015; Soto-Sánchez et al., 2017) and the TRN shapes the selectivity of thalamic responses (Cotillon-Williams et al., 2008; Vantomme et al., 2020). Therefore, an important future direction will be to include structured connectivity (e.g., based on the similarity of preferred stimulus tuning), to study circuit mechanisms of TRN regulation of thalamic selectivity.

Our sensitivity analysis characterized excitation-inhibition balance as a key effective parameter regulating thalamic dynamics and computation, with preferential sensitivity to perturbations involving RE neurons. The TRN has emerged as a key site of vulnerability associated with neurodevelopmental disorders and as a target for therapeutics (Krol et al., 2018; Huguenard and McCormick, 2007; Fagerberg et al., 2014; Ritter-Makinson et al., 2019; Ahrens et al., 2015; Wells et al., 2016). Incorporation of additional biophysical processes in the model will likely be important for simulating effects of disease and pharmacology, to link cellular and synaptic perturbations to deficits in perceptual and cognitive functions.

Finally, future studies can incorporate biophysically grounded models of thalamus into large-scale brain models of cognitive functions such as attentional control and decision making (Murray et al., 2017; Jaramillo et al., 2019). The present circuit model can be embedded in networks with long-range interactions involving thalamic, cortical and basal ganglia circuits, to gain further insight into the distributed computational mechanisms of attentional function (Saalmann and Kastner, 2011; Sherman, 2016; Halassa and Kastner, 2017; Nakajima and Halassa, 2017; Rikhye et al., 2018; Schmitt et al., 2017; Krauzlis et al., 2018). Our present study thereby provides a foundation for computational modeling of cognitive functions involving the interactions of thalamic reticular circuits and other brain circuits.

Acknowledgements

This research was supported by NIH grants R01MH112746 (JDM), R01MH107680 and R01NS098505 (MMH); NSERC (NHL); and the Swartz Foundation (QLG). We thank members of the Murray and Halassa labs for helpful discussions and feedback on the manuscript.

Author Contributions

Conceptualization: QLG, NHL, MMH, JDM; Methodology: QLG, NHL, JDM; Software: QLG, NHL; Formal Analysis: QLG, NHL; Writing – Original Draft: QLG, NHL, JDM; Writing – Review & Editing: QLG, NHL, MMH, JDM; Visualization: QLG; Supervision: JDM; Project Administration: JDM; Funding Acquisition: JDM.

Methods

Circuit Model

The thalamic reticular circuit model consists of $N_{\mathrm{TC}} = 1000$ excitatory thalamocortical (TC) neurons and $N_{\mathrm{RE}} = 1000$ inhibitory reticular (RE) neurons. TC and RE neurons are interconnected through sparse and random synaptic projections, without projections between neurons of the same cell type, with probability of connection $p_{\mathrm{TC}\to\mathrm{RE}} = p_{\mathrm{RE}\to\mathrm{TC}} = 0.01$ and $p_{\mathrm{TC}\to\mathrm{TC}} = p_{\mathrm{RE}\to\mathrm{RE}} = 0$ (Jones, 2012; Hou et al., 2016). Both TC and RE neurons receive external excitatory inputs, and RE neurons additionally receives external inhibitory inputs. All excitatory synaptic connections are mediated by α-amino-3-hydroxy-5-methyl-4-isoxazolepropionic acid receptor (AMPAR) conductances, and all inhibitory synaptic connections are mediated by γ-aminobutyric acid type-A receptors ($\mathrm{GABA_A R}$) conductances, following:

$$\begin{aligned} I_{\mathrm{syn}}^{x,i} &= g_{\mathrm{syn}}^{x,i}\, s_{\mathrm{syn}}^{x,i}\, (v^{x,i} - V_{\mathrm{syn}}) \\ \frac{d}{dt} s_{\mathrm{syn}}^{x,i} &= -s_{\mathrm{syn}}^{x,i}/\tau_{\mathrm{syn}}, \end{aligned} \tag{1}$$

where x refers to the target neuron group (TC or RE), i refers to the neuron index within the group, and *syn* refers to the synapse type (AMPA or $\mathrm{GABA_A}$). $V_{\mathrm{AMPA}} = 0$ mV, $V_{\mathrm{GABA}} = -80$ mV, $\tau_{\mathrm{AMPA}} = 2.5$ ms, and $\tau_{\mathrm{GABA}} = 10$ ms are the reversal potentials and synaptic timescales of AMPAR and GABAR.

To produce distributions of firing rate and burst rate comparable to experimental observations, the synaptic conductances of external inputs $g_{\mathrm{syn,ext}}^{x,i}$ are set to be heterogeneous, with conductance strengths following a log-normal distribution with mean $\bar{g}_{\mathrm{syn,ext}}^{x}$ and standard deviation $\sqrt{\bar{g}_{\mathrm{syn,ext}}^{x}}\sigma_{\mathrm{syn,ext}}^{x}$. The extent of heterogeneity of the external inputs and the neuronal firing rates in the circuit is thereby shaped by $\sigma_{\mathrm{syn,ext}}^{x}$. The parameters for external inputs are $\bar{g}_{\mathrm{AMPA,ext}}^{\mathrm{TC}} = 0.018$ mS/cm^2, $\bar{g}_{\mathrm{AMPA,ext}}^{\mathrm{RE}} = 0.0128$ mS/cm^2, $\bar{g}_{\mathrm{GABA}}^{\mathrm{RE}} = 0.0064$ mS/cm^2, $\sigma_{\mathrm{AMPA,ext}}^{\mathrm{TC}} = 0.4$, $\sigma_{\mathrm{AMPA,ext}}^{RE} = 0.3$, and $\sigma_{\mathrm{GABA,ext}}^{RE} = 0.15$. In **Figure 3**, $\bar{g}_{\mathrm{syn,ext}}^{x}$ is instead varied so that mean firing rate is fixed around 11 Hz for TC neurons and 16 Hz for RE neurons. The synaptic conductances for connections between TC and RE neurons are constant, with $\bar{g}_{\mathrm{AMPA}}^{\mathrm{TC}\to\mathrm{RE}} = 0.005$ mS/cm^2 and $\bar{g}_{\mathrm{GABA}}^{\mathrm{RE}\to\mathrm{TC}} = 0.05$ mS/cm^2.

TC Neuronal Model

The TC neuron is modeled by a single-compartment Hodgkin-Huxley model, with a minimal set of active conductances sufficient o endow the neuron with characteristic the tonic and burst spiking dynamics (**Figure S1**). The model is similar to prior models of TC neurons (Destexhe et al., 1993b;a), and specific TC channel conductance equations used here were adapted from prior TC neuron modeling (Destexhe et al., 1993a; Golomb et al., 1996). In all equations below describing neuronal currents, membrane potential has the unit of millivolt (mV), and temperature factors T_{adj} were set with temperature $T = 36°\mathrm{C}$.

The membrane potential of the TC neuron is governed by the following dynamics:

$$C_m \frac{dv^{\mathrm{TC}}}{dt} = -I_{\mathrm{L}}^{\mathrm{TC}} - I_{\mathrm{Na}}^{\mathrm{TC}} - I_{\mathrm{K}}^{\mathrm{TC}} - I_{\mathrm{CaT}}^{\mathrm{TC}} - I_{\mathrm{h}}^{\mathrm{TC}} - I_{\mathrm{GABA}}^{\mathrm{TC}\leftarrow\mathrm{RE}} - I_{\mathrm{AMPA}}^{\mathrm{TC}\leftarrow\mathrm{ext}} + I_{\mathrm{inj}}^{\mathrm{TC}}, \tag{2}$$

where $I_{\mathrm{inj}}^{\mathrm{TC}}$ is any injected current input, and the leak current is $I_{\mathrm{L}}^{\mathrm{TC}} = g_{\mathrm{L}}^{\mathrm{TC}}(v^{\mathrm{TC}} - V_{\mathrm{L}}^{\mathrm{TC}})$ with $g_{\mathrm{L}}^{\mathrm{TC}} = 0.05$ mS/cm^2 and $V_{\mathrm{L}}^{\mathrm{TC}} =$

-90 mV. The Na^+ current dynamics are given by :

$$
\begin{aligned}
I_{\mathrm{Na}}^{\mathrm{TC}} &= g_{\mathrm{Na}}^{\mathrm{TC}} \left(m_{\mathrm{Na}}^{\mathrm{TC}}\right)^3 h_{\mathrm{Na}}^{\mathrm{TC}} \left(v^{\mathrm{TC}} - V_{\mathrm{Na}}\right) \\
\frac{dm_{\mathrm{Na}}^{\mathrm{TC}}}{dt} &= \left[a_{m,\mathrm{Na}}^{\mathrm{TC}} \left(1 - m_{\mathrm{Na}}^{\mathrm{TC}}\right) - b_{m,\mathrm{Na}}^{\mathrm{TC}} m_{\mathrm{Na}}^{\mathrm{TC}}\right] \cdot T_{\mathrm{adj}}^{\mathrm{Na,K}} \\
\frac{dh_{\mathrm{Na}}^{\mathrm{TC}}}{dt} &= \left[a_{h,\mathrm{Na}}^{\mathrm{TC}} \left(1 - h_{\mathrm{Na}}^{\mathrm{TC}}\right) - b_{h,\mathrm{Na}}^{\mathrm{TC}} h_{\mathrm{Na}}^{\mathrm{TC}}\right] \cdot T_{\mathrm{adj}}^{\mathrm{Na,K}} \\
a_{m,\mathrm{Na}}^{\mathrm{TC}} &= -0.32 \frac{v^{\mathrm{TC}} - V_T - 13}{\exp\left[-\left(v^{\mathrm{TC}} - V_T - 13\right)/4\right] - 1} \\
b_{m,\mathrm{Na}}^{\mathrm{TC}} &= 0.28 \frac{v^{\mathrm{TC}} - V_T - 40}{\exp\left[-\left(v^{\mathrm{TC}} - V_T - 40\right)/5\right] - 1} \\
a_{h,\mathrm{Na}}^{\mathrm{TC}} &= 0.128 \mathrm{e}^{-\left(v^{\mathrm{TC}} - V_T - 17\right)/18} \\
b_{h,\mathrm{Na}}^{\mathrm{TC}} &= \frac{4}{\exp\left[-\left(v^{\mathrm{TC}} - V_T - 40\right)/5\right] + 1}.
\end{aligned}
\tag{3}
$$

where $g_{\mathrm{Na}}^{\mathrm{TC}} = 30$ mS/cm^2, $V_{Na} = 50$ mV, and the spike adjusting threshold $V_T = -55$ mV. The temperature factor is given by $T_{\mathrm{adj}}^{\mathrm{Na,K}} = 3^{(\mathrm{T}-36)/10}$.

The K^+ current dynamics are given by:

$$
\begin{aligned}
I_{\mathrm{K}}^{\mathrm{TC}} &= g_{\mathrm{K}}^{\mathrm{TC}} (n_{\mathrm{K}}^{\mathrm{TC}})^4 (v^{\mathrm{TC}} - V_{\mathrm{K}}) \\
\frac{dn_{\mathrm{K}}^{\mathrm{TC}}}{dt} &= \left[a_{n,\mathrm{K}}^{\mathrm{TC}} \left(1 - n_{\mathrm{K}}^{\mathrm{TC}}\right) - b_{n,\mathrm{K}}^{\mathrm{TC}} n_{\mathrm{K}}^{\mathrm{TC}}\right] \cdot T_{\mathrm{adj}}^{Na,\mathrm{K}} \\
a_{n,\mathrm{K}}^{\mathrm{TC}} &= -0.32 \frac{v^{\mathrm{TC}} - V_T - 15}{\exp\left[-\left(v^{\mathrm{TC}} - V_T - 15\right)/5\right] - 1} \\
b_{n,\mathrm{K}}^{\mathrm{TC}} &= 0.5 \mathrm{e}^{-\left(v^{\mathrm{TC}} - V_T - 10\right)/40},
\end{aligned}
\tag{4}
$$

where $g_{\mathrm{K}}^{\mathrm{TC}} = 2$ mS/cm^2, and $V_{\mathrm{K}} = -95$ mV.

The low-threshold Ca^{2+} current dynamics are given by:

$$
\begin{aligned}
I_{\mathrm{Ca}}^{\mathrm{TC}} &= g_{\mathrm{Ca}}^{\mathrm{TC}} \left(m_{\mathrm{Ca}}^{\mathrm{TC}}\right)^3 h_{\mathrm{Ca}}^{\mathrm{TC}} \left(v^{\mathrm{TC}} - V_{\mathrm{Ca}}\right) \\
\frac{dm_{\mathrm{Ca}}^{\mathrm{TC}}}{dt} &= \left(m_{\infty,\mathrm{Ca}}^{\mathrm{TC}} - m_{\mathrm{Ca}}^{\mathrm{TC}}\right) / \tau_{m,\mathrm{Ca}}^{\mathrm{TC}} \\
\frac{dh_{1,\mathrm{Ca}}^{\mathrm{TC}}}{dt} &= a_{h1,\mathrm{Ca}}^{\mathrm{TC}} \left(1 - h_{1,\mathrm{Ca}}^{\mathrm{TC}} - h_{2,\mathrm{Ca}}^{\mathrm{TC}}\right) - b_{h1,\mathrm{Ca}}^{\mathrm{TC}} h_{1,\mathrm{Ca}}^{\mathrm{TC}} \\
\frac{dh_{2,\mathrm{Ca}}^{\mathrm{TC}}}{dt} &= b_{h2,\mathrm{Ca}}^{\mathrm{TC}} \left(1 - h_{1,\mathrm{Ca}}^{\mathrm{TC}} - h_{2,\mathrm{Ca}}^{\mathrm{TC}}\right) - a_{h2,\mathrm{Ca}}^{\mathrm{TC}} h_{2,\mathrm{Ca}}^{\mathrm{TC}} \\
m_{\infty,\mathrm{Ca}}^{\mathrm{TC}} &= \frac{1}{1 + \exp\left[-\left(v^{\mathrm{TC}} + 65\right)/7.8\right]} \\
\tau_{m,\mathrm{Ca}}^{\mathrm{TC}} &= \frac{1}{T_{\mathrm{adj},m}^{\mathrm{Ca,TC}}} m_{\infty,\mathrm{Ca}}^{\mathrm{TC}} \cdot \left(1 + \exp\left[-\left(v^{\mathrm{TC}} + 30.8\right)/13.5\right]\right) \\
\mathbb{K}_{h,\mathrm{Ca}}^{\mathrm{TC}} &= \sqrt{0.25 + \exp\left(v^{\mathrm{TC}} + 85.5\right)/6.3} - 0.5 \\
a_{h1,\mathrm{Ca}}^{\mathrm{TC}} &= \exp\left[-\left(v^{\mathrm{TC}} + 162.3\right)/17.8\right] \cdot T_{\mathrm{adj},h}^{Ca,\mathrm{TC}} \\
b_{h1,\mathrm{Ca}}^{\mathrm{TC}} &= a_{h1,\mathrm{Ca}}^{\mathrm{TC}} \mathbb{K}_{h,\mathrm{Ca}}^{\mathrm{TC}} \\
a_{h2,\mathrm{Ca}}^{\mathrm{TC}} &= \frac{1 + \exp\left[v^{\mathrm{TC}} + 39.4\right]/30}{240 \cdot \left(1 + \mathbb{K}_{h,\mathrm{Ca}}^{\mathrm{TC}}\right)} \cdot T_{\mathrm{adj},h}^{\mathrm{Ca,TC}} \\
b_{h2,\mathrm{Ca}}^{\mathrm{TC}} &= a_{h2,\mathrm{Ca}}^{\mathrm{TC}} \mathbb{K}_{h,\mathrm{Ca}}^{\mathrm{TC}} \\
\frac{d[\mathrm{Ca}]^{\mathrm{TC}}}{dt} &= -\left[-a_{\mathrm{Ca}} I_{\mathrm{Ca}}^{\mathrm{TC}}\right]_+ - K_{T,\mathrm{Ca}} \frac{[\mathrm{Ca}]^{\mathrm{TC}}}{[\mathrm{Ca}]^{\mathrm{TC}} + K_{D,\mathrm{Ca}}},
\end{aligned}
\tag{5}
$$

where $g_{\mathrm{Ca}}^{\mathrm{TC}} = 1.4$ mS/cm^2, and $V_{\mathrm{Ca}} = 120$ mV. The temperature factors $T_{\mathrm{adj},m}^{\mathrm{Ca,TC}} = 5^{(\mathrm{T}-24)/10}$ and $T_{\mathrm{adj},h}^{\mathrm{Ca,TC}} = 3^{(\mathrm{T}-24)/10}$. The gating kinetics was adjusted to 36 °C. Parameters for the Ca^{2+} kinetics, $a_{\mathrm{Ca}} = 1/(2 \times 96489\ \mathrm{Cmol}^{-1} \times 1\mu\mathrm{m})$, $K_{T,\mathrm{Ca}} =$

0.1μM/ms, and $K_{D,\mathrm{Ca}} = 0.1\mu$M.
I_h^{TC} is modeled as a single-variable kinetic scheme with the dependence of its activation on voltage and intracellular Ca^{2+}. The kinetic equations are as following:

$$
\begin{aligned}
I_h^{\mathrm{TC}} &= g_h^{\mathrm{TC}} m_h^{\mathrm{TC}} (v^{\mathrm{TC}} - V_h) \\
m_h^{\mathrm{TC}} &= \mathrm{O}_{1,h}^{\mathrm{TC}} + g_{\mathrm{inc},h}^{\mathrm{TC}} \mathrm{O}_{2,h}^{\mathrm{TC}} \\
\frac{d}{dt}\mathrm{O}_{1,h}^{\mathrm{TC}} &= a_h^{\mathrm{TC}}(1 - \mathrm{O}_{1,h}^{\mathrm{TC}} - \mathrm{O}_{2,h}^{\mathrm{TC}}) - b_h^{\mathrm{TC}}\mathrm{O}_{1,h}^{\mathrm{TC}} + k_{4,h}^{\mathrm{TC}}\mathrm{O}_{2,h}^{\mathrm{TC}} - k_{3,h}^{\mathrm{TC}}\mathrm{P}_h^{\mathrm{TC}}\mathrm{O}_{1,h}^{\mathrm{TC}} \\
\frac{d}{dt}\mathrm{O}_{2,h}^{\mathrm{TC}} &= -k_{4,h}^{\mathrm{TC}}\mathrm{O}_{2,h}^{\mathrm{TC}} + k_{3,h}^{\mathrm{TC}}\mathrm{P}_h^{\mathrm{TC}}\mathrm{O}_{1,h}^{\mathrm{TC}} \\
\frac{d}{dt}\mathrm{P}_h^{\mathrm{TC}} &= -k_{2,h}^{\mathrm{TC}}\mathrm{P}_h^{\mathrm{TC}} + k_{1,h}^{\mathrm{TC}}(Ca^{\mathrm{TC}})^4(1 - \mathrm{P}_h^{\mathrm{TC}}) \\
a_h^{\mathrm{TC}} &= H_{\infty,h}^{\mathrm{TC}}/\tau_h^{\mathrm{TC}} \\
b_h^{\mathrm{TC}} &= (1 - H_{\infty,h}^{\mathrm{TC}})/\tau_h^{\mathrm{TC}} \\
H_{\infty,h}^{\mathrm{TC}} &= \frac{1}{1 + \exp[(v^{\mathrm{TC}} + 75)/5.5]} \\
\tau_h^{\mathrm{TC}} &= \frac{1}{T_{\mathrm{adj},m}^{h,\mathrm{TC}}} \cdot (20 + \frac{1000}{\exp[(v^{\mathrm{TC}} + 71.5)/14.2] + \exp[(v^{\mathrm{TC}} + 89)/11.6]}),
\end{aligned}
\tag{6}
$$

where $g_h^{\mathrm{TC}} = 0.05$ mS/cm^2, $V_h = -43$ mV, and $g_{\mathrm{inc},h}^{\mathrm{TC}} = 2$. According to the channel properties, the reaction rates are $k_{1,h}^{\mathrm{TC}} = 25\ \mu\mathrm{M}^{-2}\mathrm{ms}^{-1}$, $k_{2,h}^{\mathrm{TC}} = 4 \times 10^{-4}\ \mathrm{ms}^{-1}$, $k_{3,h}^{\mathrm{TC}} = 0.1\ \mathrm{ms}^{-1}$, and $k_{3,h}^{\mathrm{TC}} = 10^{-3}\ \mathrm{ms}^{-1}$.

RE Neuronal Model

The RE neuron is also modeled by a single-compartment Hodgkin-Huxley model, with the specific channel conductance equations adapted from prior RE neuron modeling (Destexhe et al., 1994; 1996).

The membrane potential of the RE neuron is governed by the following dynamics:

$$
\begin{aligned}
C_m \frac{dv^{\mathrm{RE}}}{dt} = &- I_{\mathrm{L}}^{\mathrm{RE}} - I_{\mathrm{Na}}^{\mathrm{RE}} - I_{\mathrm{K}}^{\mathrm{RE}} - I_{\mathrm{CaT}}^{\mathrm{RE}} - I_{\mathrm{KCa}}^{\mathrm{RE}} - I_{\mathrm{CaN}}^{\mathrm{RE}} \\
&- I_{\mathrm{AMPA}}^{\mathrm{RE}\leftarrow\mathrm{TC}} - I_{\mathrm{AMPA}}^{\mathrm{RE}\leftarrow\mathrm{ext}} - I_{\mathrm{GABA}}^{\mathrm{RE}\leftarrow\mathrm{ext}} + I_{\mathrm{inj}}^{\mathrm{RE}},
\end{aligned}
\tag{7}
$$

where $I_{\mathrm{inj}}^{\mathrm{RE}}$ is any injected current input, and the leak current is $I_{\mathrm{L}}^{RE} = g_{\mathrm{L}}^{\mathrm{RE}}(v^{\mathrm{RE}} - V_{\mathrm{L}}^{\mathrm{RE}})$ with $g_{\mathrm{L}}^{\mathrm{RE}} = 0.05$ mS/cm^2 and $V_{\mathrm{L}}^{\mathrm{RE}} = -80$ mV. Here $I_{\mathrm{Na}}^{\mathrm{RE}}$ and $I_{\mathrm{K}}^{\mathrm{RE}}$ have the form as Eq. (3) and Eq. (4) respectively, with $g_{\mathrm{Na}}^{\mathrm{RE}} = 100$ mS/cm^2 and $g_{\mathrm{K}}^{\mathrm{RE}} = 10$ mS/cm^2. The low-threshold Ca^{2+} current $I_{\mathrm{Ca}}^{\mathrm{RE}}$ has the following form:

$$
\begin{aligned}
I_{\mathrm{Ca}}^{\mathrm{RE}} &= g_{\mathrm{Ca}}^{\mathrm{RE}}(m_{\mathrm{Ca}}^{\mathrm{RE}})^2 h_{\mathrm{Ca}}^{\mathrm{RE}}(v^{\mathrm{RE}} - V_{\mathrm{Ca}}) \\
\frac{dm_{\mathrm{Ca}}^{\mathrm{RE}}}{dt} &= T_{\mathrm{adj},m}^{\mathrm{Ca,RE}} \cdot (m_{\infty,\mathrm{Ca}}^{\mathrm{RE}} - m_{\mathrm{Ca}}^{\mathrm{RE}})/\tau_{m,Ca}^{RE} \\
\frac{dh_{\mathrm{Ca}}^{\mathrm{RE}}}{dt} &= T_{\mathrm{adj},h}^{\mathrm{Ca,RE}} \cdot (h_{\infty,\mathrm{Ca}}^{\mathrm{RE}} - h_{Ca}^{RE})/\tau_{h,Ca}^{RE} \\
m_{\infty,\mathrm{Ca}}^{\mathrm{RE}} &= \frac{1}{1 + \exp[-(v^{\mathrm{TC}} + 52)/7.4]} \\
\tau_{m,\mathrm{Ca}}^{\mathrm{RE}} &= 3 + \frac{1}{\exp[(v^{\mathrm{RE}} + 27)/10] + \exp[-(v^{\mathrm{RE}+102}/15)]} \\
h_{\infty,\mathrm{Ca}}^{\mathrm{RE}} &= \frac{1}{1 + \exp[-(v^{\mathrm{TC}} + 80)/5.0]} \\
\tau_{h,\mathrm{Ca}}^{RE} &= 85 + \frac{1}{\exp[(v^{\mathrm{RE}} + 48)/4] + \exp[-(v^{\mathrm{RE}+407}/50)]} \\
\frac{d\mathrm{Ca}^{\mathrm{RE}}}{dt} &= -(-a_{\mathrm{Ca}}^{\mathrm{RE}} I_{\mathrm{Ca}}^{\mathrm{RE}})_+ - (\mathrm{Ca}^{\mathrm{RE}} - \mathrm{Ca}_{\infty}^{\mathrm{RE}})/\tau_{\mathrm{Ca}}^{\mathrm{RE}},
\end{aligned}
\tag{8}
$$

where $g_{\mathrm{Ca}}^{\mathrm{RE}} = 2.1\ \mathrm{mS/cm^2}$. The temperature adjusting terms $T_{\mathrm{adj},m}^{\mathrm{Ca,RE}} = 5^{(\mathrm{T}-24)/10}$ and $T_{\mathrm{adj},m}^{\mathrm{Ca,RE}} = 3^{(\mathrm{T}-24)/10}$. The gating kinetics was adjusted to 36 °C. Parameters for the Calcium kinetics, $a_{\mathrm{Ca}}^{\mathrm{RE}} = 1/(2 \times 96489\ \mathrm{Cmol^{-1}} \times 1\mu\mathrm{m})$, $\mathrm{Ca}_{\infty}^{RE} = 0.24\ \mu\mathrm{M}$, and $\tau_{\mathrm{Ca}}^{\mathrm{RE}} = 5$ ms.

The Ca^{2+}-dependent K+ current is described as:

$$\begin{aligned} I_{\mathrm{KCa}}^{\mathrm{RE}} &= g_{\mathrm{KCa}}^{RE}(m_{\mathrm{KCa}}^{RE})^2(v^{\mathrm{RE}} - V_{\mathrm{K}}) \\ \frac{dm_{\mathrm{KCa}}^{\mathrm{RE}}}{dt} &= (m_{\infty,\mathrm{KCa}}^{\mathrm{RE}} - m_{\mathrm{KCa}}^{\mathrm{RE}})/\tau_{\mathrm{KCa}}^{\mathrm{RE}} \\ m_{\infty,\mathrm{KCa}}^{\mathrm{RE}} &= a_{m,\mathrm{KCa}}^{\mathrm{RE}}(\mathrm{Ca}^{\mathrm{RE}})^2/[a_{m,\mathrm{KCa}}^{\mathrm{RE}}(\mathrm{Ca}^{\mathrm{RE}})^2 + b_{m,\mathrm{KCa}}^{\mathrm{RE}}] \\ \tau_{\mathrm{KCa}}^{\mathrm{RE}} &= \frac{1}{T_{\mathrm{adj},m}^{\mathrm{KCa,RE}}} \frac{1}{a_{m,\mathrm{KCa}}^{\mathrm{RE}}(\mathrm{Ca}^{\mathrm{RE}})^2 + b_{m,\mathrm{KCa}}^{\mathrm{RE}}}, \end{aligned} \tag{9}$$

where $g_{\mathrm{KCa}}^{\mathrm{RE}} = 10\ \mathrm{mS/cm^2}$, $a_{m,\mathrm{KCa}}^{\mathrm{RE}} = 48\ \mathrm{ms^{-1}mM^2}$, and $b_{m,\mathrm{KCa}}^{\mathrm{RE}} = 0.03\ \mathrm{ms^{-1}}$. The temperature adjusting term is $T_{\mathrm{adj},m}^{\mathrm{KCa,RE}} = 3^{(\mathrm{T}-22)/10}$.

The Ca^{2+}-dependent nonspecific cation current follows the equation:

$$\begin{aligned} I_{\mathrm{CaN}}^{\mathrm{RE}} &= g_{\mathrm{CaN}}^{RE}(m_{\mathrm{CaN}}^{\mathrm{RE}})^2(v^{\mathrm{RE}} - V_{\mathrm{CaN}}) \\ \frac{dm_{\mathrm{CaN}}^{\mathrm{RE}}}{dt} &= (m_{\infty,\mathrm{CaN}}^{\mathrm{RE}} - m_{\mathrm{CaN}}^{\mathrm{RE}})/\tau_{\mathrm{CaN}}^{\mathrm{RE}} \\ m_{\infty,\mathrm{CaN}}^{\mathrm{RE}} &= a_{m,\mathrm{CaN}}^{\mathrm{RE}}(\mathrm{Ca}^{\mathrm{RE}})^2/[a_{m,\mathrm{CaN}}^{\mathrm{RE}}(\mathrm{Ca}^{\mathrm{RE}})^2 + b_{m,\mathrm{CaN}}^{\mathrm{RE}}] \\ \tau_{\mathrm{CaN}}^{\mathrm{RE}} &= \frac{1}{T_{\mathrm{adj},m}^{\mathrm{CaN,RE}}} \frac{1}{a_{m,\mathrm{CaN}}^{\mathrm{RE}}(\mathrm{Ca}^{\mathrm{RE}})^2 + b_{m,\mathrm{CaN}}^{\mathrm{RE}}}, \end{aligned} \tag{10}$$

where $g_{\mathrm{CaN}}^{\mathrm{RE}} = 0.25\ \mathrm{mS/cm^2}$, $V_{\mathrm{CaN}} = -20\ \mathrm{mV}$, $a_{m,\mathrm{CaN}}^{\mathrm{RE}} = 20\ \mathrm{ms^{-1}mM^{-3}})^2$, and $b_{m,\mathrm{CaN}}^{\mathrm{RE}} = 0.002\ \mathrm{ms^{-1}}$, and the temperature adjusting term $T_{\mathrm{adj},m}^{\mathrm{CaN,RE}} = 3^{(\mathrm{T}-22)/10}$.

Top-down and Stimulus Inputs

Top-down inputs are stimulated as Poisson-distributed spike trains, of a given rate, driving either $\mathrm{GABA_A}$ or AMPA synapses on either RE or TC neurons. The external spike trains are generated by a Poisson process with rate $\Gamma_{\mathrm{syn}}^{x} \nu_{\mathrm{syn}}^{x}$ for $\mathrm{syn} = \mathrm{AMPA}$, GABA and $x = \mathrm{TC}$, RE. Here, $\Gamma_{\mathrm{syn}}^{x}$ is the factor denoting the strength of the top-down attentional modulation, with $\Gamma_{\mathrm{syn}}^{x} = 1$ during the baseline state. We set $\nu_{\mathrm{AMPA}}^{\mathrm{TC}} = 400$ (sp/s), $\nu_{\mathrm{AMPA}}^{\mathrm{RE}} = 400$ (sp/s) and $\nu_{\mathrm{GABA}}^{\mathrm{RE}} = 400$ (sp/s) to obtain the the mean firing rate is around 11 (sp/s) for TC neurons and 16 (sp/s) for RE neurons.

For parsimony, stimulus inputs are generally simulated as direct current inputs to TC neurons. The probability of a TC neuron receiving a stimulus input is random with probability $p = 0.5$ to reflect stimulus specificity on sensory inputs to TC neurons. In most figures, stimulus inputs are unstructured with equal strength to all recipient TC neurons. However, in **Figure 7** and corresponding parts of **Figure 8** (S^{dis},S^{cong},S^{inco}), stimuli inputs are structured across neuron index to reflect tuned sensory inputs in discrimination tasks, with a Gaussian wave of width $\sigma = 30$ neurons around the mean (and extending past neuron 1 to neuron 1000 and vice versa). The two inputs for discrimination have a difference in mean location by 30 neurons.

Measures of circuit dynamics

In **Figures 2**, **8**, **S1**, and **S5**, we characterized aspects of circuit spiking dynamics and their dependence on model parameters. A burst (**Figures 2, S1**) of a neuron is defined as multiple (at least two) spikes with an interspike-interval

(ISI) of less than 20 ms, preceded by a long period of 100 ms with no spiking. This definition of bursting is similar to prior definitions used in electrophysiological studies of thalamus (Halassa et al., 2011; Wells et al., 2016). Spindle probability is defined as the probability the spindle power reaches a threshold (**Figures 8, S5**). The spindle power is defined as the power within 9 to 15 Hz band-pass filtered from the power spectrum of population spiking activity.

The awake state regime can be defined by two curves in the parameter space of **Figures 2,S2**. The orange line defines the upper bound before which the spontaneous activity becomes synchonrous (**Figure 2I**), and the purple line defines the lower bound for RE activation to generate an evoked spindle-like response (**Figure 2J**). The two lines are defined as the equipotential lines where the maximum power spectral density in either case reach a certain threshold. The threshold is chosen by considering the first column in (**Figure 2J**), where TC neurons do not project to RE neurons. Since any oscillations in the current regime of the circuit model come from reverberation between TC and RE neurons, the circuits in the first column in (**Figure 2J**) are in the asynchronous regime. The threshold is defined as the mean plus twice the standard deviation of maximum power spectral density across that column.

Reduced Two-variable Mean-field Model

For the dynamical systems analysis of **Figure 5**, we reduced the thalamic circuit to a two-variable mean-field description, with one dynamical variable representing the activity of each of the excitatory and inhibitory populations (as in Wong and Wang (2006); Jaramillo et al. (2019)). The synaptic gating variables of the TC and RE populations (s^α, $\alpha = \mathrm{TC}, \mathrm{RE}$) follow:

$$\frac{d}{dt}s^\alpha = -\frac{s^\alpha}{\tau^\alpha} + F^\alpha(I^\alpha) \tag{11}$$

where $\tau^{\mathrm{TC}} = 2.5$ ms is the time constant of fast AMPA synapses, and $\tau^{\mathrm{RE}} = 10$ ms is the time constant of $\mathrm{GABA_A}$ synapses. $F^\alpha(\cdot)$ describes the frequency-current (F-I) curve relation used in prior studies (Abbott and Chance, 2005; Wong and Wang, 2006; Murray et al., 2017):

$$r^\alpha = F^\alpha(I^\alpha) = \frac{a^\alpha I^\alpha - b^\alpha}{1 - \exp\left[-c^\alpha(a^\alpha I^\alpha - b^\alpha)\right]}. \tag{12}$$

We obtained parameters for the F-I curves by fitting Equation 12 to simulated F-I curves of our Hogkin-Huxley neuron models as shown in **Figure. 5B**. Neuronal parameters used with $a^{\mathrm{TC}} = 40.81\ (\mathrm{sp/s}) \cdot (\mu A/\mathrm{cm}^2)^{-1}$, $b^{\mathrm{TC}} = 34.54$ (sp/s), and $c^{\mathrm{TC}} = 0.107$ s for TC population, as well as $a^{\mathrm{RE}} = 25.97\ (\mathrm{sp/s}) \cdot (\mu A/\mathrm{cm}^2)^{-1}$, $b^{\mathrm{RE}} = -3.91$ (sp/s), and $c^{\mathrm{RE}} = 0.222$ s for RE population.

The input currents to the TC and RE populations are given by:

$$\begin{cases} I^{\mathrm{TC}} = -J_{\mathrm{GABA}} s^{\mathrm{RE}} + I^{\mathrm{TC}}_{\mathrm{Bg}} + I^{\mathrm{TC}}_{\mathrm{Stim}}, \\ I^{\mathrm{RE}} = J_{\mathrm{AMPA}} s^{\mathrm{TC}} + I^{\mathrm{RE}}_{\mathrm{Bg}}, \end{cases} \tag{13}$$

where I^α_{Bg} is the background input, and $I^{\mathrm{TC}}_{\mathrm{Stim}}$ is the stimulus input, J_{AMPA} is the coupling strength from TC to RE, and J_{GABA} is the coupling strength from RE to TC. Here, we chose the coupling strengths in the mean-field model to be consistent with the spiking circuit model. In the spiking circuit, each TC (RE) neuron receives 10 RE (TC) connections on average with synaptic conductance $\bar{g}^{TRN->TC}_{GABA} = 0.05\ \mathrm{mS/cm}^2$ ($\bar{g}^{TC->TRN}_{AMPA} = 0.005\ \mathrm{mS/cm}^2$). Taking into account the reversal potentials of the AMPA and GABA synapses to estimate approximate ranges of currents, we set $J_{\mathrm{AMPA}} = 4.0\ (\mu A/\mathrm{cm}^2)$ and $J_{\mathrm{GABA}} = 4.5\ (\mu A/\mathrm{cm}^2)$. Finally, the background inputs I^α_{Bg} were set so that the TC firing rate is 10 (sp/s) and RE firing rate is 15 (sp/s), in line with the spiking circuit model, with values $I^{\mathrm{TC}}_{\mathrm{Bg}} = 1.552\ (\mu A/\mathrm{cm}^2)$ and $I^{\mathrm{RE}}_{\mathrm{Bg}} = 0.305\ (\mu A/\mathrm{cm}^2)$.

From eq. (13), we can derive

$$\begin{cases} s^{\mathrm{TC}} = \dfrac{I^{\mathrm{RE}} - I^{\mathrm{RE}}_{\mathrm{Bg}}}{J_{\mathrm{AMPA}}}, \\ s^{\mathrm{RE}} = -\dfrac{I^{\mathrm{TC}} - I^{\mathrm{TC}}_{\mathrm{Bg}} - I^{\mathrm{TC}}_{\mathrm{Stim}}}{J_{\mathrm{GABA}}}. \end{cases}$$

Therefore, eq. (11) can be expressed as

$$\begin{cases} \frac{d}{dt}I^{\mathrm{TC}} = -\frac{I^{\mathrm{TC}}}{\tau^{\mathrm{RE}}} + \frac{I^{\mathrm{TC}}_{\mathrm{Bg}} + I^{\mathrm{TC}}_{\mathrm{Stim}}}{\tau^{\mathrm{RE}}} - J_{\mathrm{GABA}}F^{\mathrm{RE}}(I^{\mathrm{RE}}), \\ \frac{d}{dt}I^{\mathrm{RE}} = -\frac{I^{\mathrm{RE}}}{\tau^{\mathrm{TC}}} + \frac{I^{\mathrm{RE}}_{\mathrm{Bg}}}{\tau^{\mathrm{TC}}} + J_{\mathrm{AMPA}}F^{\mathrm{TC}}(I^{\mathrm{TC}}), \end{cases} \tag{14}$$

with steady-state solution

$$\begin{cases} s^{\mathrm{TC}}_0 = \tau^{\mathrm{TC}}F^{\mathrm{TC}}(I^{\mathrm{TC}}_0) = \tau^{\mathrm{TC}}F^{\mathrm{TC}}(s^{\mathrm{TC}}_0, s^{\mathrm{RE}}_0) \\ s^{\mathrm{RE}}_0 = \tau^{\mathrm{RE}}F^{\mathrm{RE}}(I^{\mathrm{RE}}_0) = \tau^{\mathrm{RE}}F^{\mathrm{RE}}(s^{\mathrm{TC}}_0, s^{\mathrm{RE}}_0). \end{cases}$$

To calculate the response gain of the circuit, we consider the impact of small increment in stimulus input δI to $I^{\mathrm{TC}}_{\mathrm{Stim}}$. The response gain of the circuit can be defined as the local slope k^{TC} for the change in TC firing rate (δr^{TC}) resulting from the stimulus increment: $\delta r^{\mathrm{TC}} \approx k^{\mathrm{TC}}\delta I$.

As a consequence of the stimulus increment δI, s^{TC}_0 and s^{RE}_0 change with increments δs^{TC} and δs^{RE}, respectively. Then we can derive the increments of the total current inputs as $\delta I^{\mathrm{TC}} = -J_{\mathrm{GABA}}\delta s^{\mathrm{RE}} + \delta I$ and $\delta I^{\mathrm{RE}} = J_{\mathrm{AMPA}}\delta s^{\mathrm{TC}}$, and the first-order linearized approximation of the F-I curve as

$$\begin{cases} F^{\mathrm{TC}}(I^{\mathrm{TC}}_0 + \delta I^{\mathrm{TC}}) \approx F^{\mathrm{TC}}(I^{\mathrm{TC}}_0) + \frac{dF^{\mathrm{TC}}(I)}{dI}\Big|_{I=I^{\mathrm{TC}}_0}(-J_{\mathrm{GABA}}\delta s^{\mathrm{RE}} + \delta I), \\ F^{\mathrm{RE}}(I^{\mathrm{RE}}_0 + \delta I^{\mathrm{RE}}) \approx F^{\mathrm{RE}}(I^{\mathrm{RE}}_0) + \frac{dF^{\mathrm{RE}}(I)}{dI}\Big|_{I=I^{\mathrm{RE}}_0}(J_{\mathrm{AMPA}}\delta s^{\mathrm{TC}}). \end{cases}$$

The resulting dynamics of the linearized systems follow

$$\frac{d}{dt}\begin{pmatrix}\delta s^{\mathrm{TC}} \\ \delta s^{\mathrm{RE}}\end{pmatrix} \approx \begin{pmatrix} -\frac{1}{\tau^{\mathrm{TC}}} & -J_{\mathrm{GABA}}\frac{dF^{\mathrm{TC}}(I)}{dI}\Big|_{I=I^{\mathrm{TC}}_0} \\ J_{\mathrm{AMPA}}\frac{dF^{\mathrm{RE}}(I)}{dI}\Big|_{I=I^{\mathrm{RE}}_0} & -\frac{1}{\tau^{\mathrm{RE}}} \end{pmatrix}\begin{pmatrix}\delta s^{\mathrm{TC}} \\ \delta s^{\mathrm{RE}}\end{pmatrix} + \begin{pmatrix}\delta I\frac{dF^{\mathrm{TC}}(I)}{dI}\Big|_{I=I^{\mathrm{TC}}_0} \\ 0\end{pmatrix},$$

from which we can derive the steady-state increments δs^{TC}_0 and δs^{RE}_0 as

$$\begin{cases} \delta s^{\mathrm{TC}}_0 = \dfrac{\tau^{\mathrm{TC}}\left(\frac{dF^{\mathrm{TC}}(I)}{dI}\Big|_{I=I^{\mathrm{TC}}_0}\right)}{1 + \tau^{\mathrm{TC}}\tau^{\mathrm{RE}}J_{\mathrm{AMPA}}J_{\mathrm{GABA}}\left(\frac{dF^{\mathrm{TC}}(I)}{dI}\Big|_{I=I^{\mathrm{TC}}_0}\right)\left(\frac{dF^{\mathrm{RE}}(I)}{dI}\Big|_{I=I^{\mathrm{RE}}_0}\right)}\delta I \\ \delta s^{\mathrm{RE}}_0 = \tau^{\mathrm{RE}}J_{\mathrm{AMPA}}\left(\frac{dF^{\mathrm{RE}}(I)}{dI}\Big|_{I=I^{\mathrm{RE}}_0}\right)\delta s^{\mathrm{TC}}_0, \end{cases}$$

and the increment of TC firing rate as

$$\begin{aligned} \delta r^{\mathrm{TC}}_0 &= F^{\mathrm{TC}}(I^{\mathrm{TC}}_0 + \delta I^{\mathrm{TC}}) - F^{\mathrm{TC}}(I^{\mathrm{TC}}_0) \approx \frac{dF^{\mathrm{TC}}(I)}{dI}\Big|_{I=I^{\mathrm{TC}}_0}(-J_{\mathrm{GABA}}\delta s^{\mathrm{RE}} + \delta I) \\ &= k^{\mathrm{TC}}(I^{\mathrm{TC}}_0, I^{\mathrm{RE}}_0) \quad \delta I \end{aligned} \tag{15}$$

where the circuit response gain $k^{\mathrm{TC}}(I^{\mathrm{TC}}_0, I^{\mathrm{RE}}_0)$ is given by

$$k^{\mathrm{TC}}(I^{\mathrm{TC}}_0, I^{\mathrm{RE}}_0) = \frac{1}{\dfrac{1}{\dfrac{dF^{\mathrm{TC}}(I)}{dI}\Big|_{I=I^{\mathrm{TC}}_0}} + \tau^{\mathrm{TC}}\tau^{\mathrm{RE}}J_{\mathrm{AMPA}}J_{\mathrm{GABA}}\left(\dfrac{dF^{\mathrm{RE}}(I)}{dI}\Big|_{I=I^{\mathrm{RE}}_0}\right)}. \tag{16}$$

Equation 16 shows that The response gain of the circuit, $k^{\mathrm{TC}}(I^{\mathrm{TC}}_0, I^{\mathrm{RE}}_0)$, depends on the first derivatives of the F-I curve of both TC and RE neurons. Note that the response gain increases when $\frac{dF^{\mathrm{TC}}(I)}{dI}\Big|_{I=I^{\mathrm{TC}}_0}$ increases or $\frac{dF^{\mathrm{RE}}(I)}{dI}\Big|_{I=I^{\mathrm{RE}}_0}$ decreases. In addition, the nonlinearity of the F-I curve (usually concave upward) makes $\frac{dF^{\mathrm{TC}}(I)}{dI}\Big|_{I=I^{\mathrm{TC}}_0}$ and $\frac{dF^{\mathrm{RE}}(I)}{dI}\Big|_{I=I^{\mathrm{RE}}_0}$ increase when the total current input I increases. Then, in the case of RE modulation, top-down modulation decreases the total input of the RE neurons for the attended modality and suppresses their firing rate, thus increasing the TC firing rate via

disinhibition. In this case, $\frac{dF^{\mathrm{TC}}(I)}{dI}\Big|_{I=I_0^{\mathrm{TC}}}$ increases and $\frac{dF^{\mathrm{RE}}(I)}{dI}\Big|_{I=I_0^{\mathrm{RE}}}$ decreases, which both increase the slope of the gain curve. In contrast, in the case of TC modulation, top-down modulation increases the total input of TC neurons and amplifies its firing rate, which in turn increases the firing rate of the RE neurons (according to Eq. (13)). As such, both $\frac{dF^{\mathrm{TC}}(I)}{dI}\Big|_{I=I_0^{\mathrm{TC}}}$ and $\frac{dF^{\mathrm{RE}}(I)}{dI}\Big|_{I=I_0^{\mathrm{RE}}}$ increase, which have opposing and partially canceling-out effects on the response gain. For interpretability and simplicity, **Figure 5** are shown in terms of the firing rates of TC and RE populations, though an equivalent description can be expressed using the synaptic gating variables in the system.

Support Vector Machine Decoder

To study how stimulus information can be read out from the spiking circuit model, and how its performance can be regulated by top-down inputs, we trained linear support vector machine (SVM) classifiers to perform detection and discrimination. All analysis is conducted using the python package scikit-learn (function linearSVM).

For each task, the firing rate of each TC neuron was calculated in a time bin after the stimuli onset on each trial. Here we used as a time bin the first 10 ms following stimulus input onset; we found that major findings were qualitatively similar if later time bins are used (not shown). The SVM classifier was trained on half of the trials (randomly selected) and the other half of the trials were used for testing and prediction. The linear SVM classifier works by first constructing an optimal hyperplane for classification, based on labeled training data, and then generating predictions of the labels on testing data. Accuracy of the decoding is assessed by comparing the predicted labels to the actual labels. The accuracy is calculated as the proportion of trials classified correctly.

Specifically, the SVM receives TC activity as input: $r^{\mathrm{TC}}(i_{\mathrm{trial}}, i_{\mathrm{stim}}, i_{\mathrm{neu}}, i_{\mathrm{mod}})$ is the firing rate of the TC neuron i_{neu} with the i_{stim}th level stimulus and i_{mod}th level top-down inhibiton to RE neurons in the i_{trial} trials. Here $i_{\mathrm{trial}} = 1, ..., 400$, $i_{\mathrm{neu}} = 1, ..., 1000$, $i_{\mathrm{stim}} = 0, 1, ..., 10$, and $i_{\mathrm{mod}} = 1, ..., 8$. Thus the total dimension of r^{TC} is $400 \times 11 \times 1000 \times 8$.

For detection, the training set consists of 200 of the trials (across all TC neurons) with no stimulus ($i_{\mathrm{stim}} = 0$ for each level of top-down modulation (with a dimension of $200 \times 1 \times 1000 \times 8$). The training set also consists of 20 trials for each level of stimulus $i_{\mathrm{stim}} = 1, ..., 10$ and each level of top-down modulation via (with a dimension of $20 \times 10 \times 1000 \times 8$). The training set thus includes half of the trials with no stimulus, and half with stimulus of various magnitudes. The testing set similarly consists of 200 trials with no stimulus (with a dimension of $200 \times 1 \times 1000 \times 8$, using trials that were not used for training), and 20 trials for each level of stimulus and top-down modulation (with a dimension of $20 \times 10 \times 1000 \times 8$, using trials that were not used for training). The labels for SVM for detection are presence (1) and absence (0) of stimulus.

For discrimination between two distinct structured inputs (input 1 and input 2) (within one modality), the training set includes 200 trials across all neurons for each level of stimulus strength (from 0 to 10) and top-down modulation via RE (from 1 to 8), for each of input 1 and 2. The dimension of the training set is thus $200 \times 11 \times 1000 \times 8 \times 2$, where the $\times 2$ accounts for input 1 and input 2. The trials not used for training have the same dimensions with the training set and is used for testing. The labels for SVM for discrimination are the identity of input 1 (1) and input 2 (0).

For congruent and incongruent discrimination across modalities, the training set includes 200 trials across levels of stimulus strength (from 0 to 10), using 2000 neurons (1000 TC neurons for each of the two modalities). Two conditions of top-down modulations are considered (for the model to attend to either modality and ignore the other) : $i_{\mathrm{mod}} = 8$ for the first modality and $i_{\mathrm{mod}} = 1$ for the second modality; and $i_{\mathrm{mod}} = 1$ for the first modality and $i_{\mathrm{mod}} = 8$ for the second modality. The dimension of the training set is thus $200 \times 11 \times 2000 \times 2$. The testing set includes the other 200 trials not used in the training set, across the same conditions as for the training set. The labels for SVM for congruent and incongruent discrimination are the identity of input 1 (1) and input 2 (0) of the attended modality.

Detection and discrimination sensitivity (**Figures 3,4,7,8**) are defined as the slope of the detection and discrimination accuracy as a function of stimulus amplitude, within the linear portion with low stimulus amplitude.

Weight Vectors for SVM, Stimulus, and Top-Down Modulations

The SVM generates a readout weight vector ($\vec{\beta}_{\mathrm{SVM}}$), with which an SVM score (S_{SVM}) can be calculated from the activity of TC neurons ($\vec{r}^{\mathrm{TC}}$):

$$S_{\mathrm{SVM}} = \vec{\beta}_{\mathrm{SVM}} \cdot \vec{r}^{\mathrm{TC}} + \beta^0_{\mathrm{SVM}} \tag{17}$$

The activity of TC neurons ($\vec{r}^{TC}$) in the training data can be fitted to a linear regression model:

$$\vec{r}^{\mathrm{TC}} = \vec{\beta}^{\mathrm{base}} + \vec{\beta}^{\mathrm{BU}} x^{\mathrm{stim}} + \vec{\beta}^{\mathrm{TD}} x^{\mathrm{mod}} + \vec{\beta}^{\mathrm{inter}} x^{\mathrm{stim}} x^{\mathrm{mod}}, \tag{18}$$

where x^{stim} is the strength of bottom-up stimulus input to TC neurons, and x^{mod} is the strength of top-down input (inhibition to RE neurons in **Figure 6**.). $\vec{\beta}^{\mathrm{BU}}$, $\vec{\beta}^{\mathrm{TD}}$, and $\vec{\beta}^{\mathrm{inter}}$ thus represent the regression coefficient weights across all neurons for bottom-up stimulus, top-down modulation, and their interaction.

The projections of the three regression weight vectors onto $\vec{\beta}_{SVM}$ can be computed. In particular, we found that the SVM weight vector is positively correlated with $\vec{\beta}^{BU}$ and $\vec{\beta}^{inter}$, but is weakly negatively correlated with $\vec{\beta}^{TD}$ (**Figures 6D,E**). This can be understood by considering the SVM score, rewriting **Equation 17** as

$$\begin{aligned} S_{\mathrm{SVM}} &= \vec{\beta}_{\mathrm{SVM}} \cdot \left(\vec{\beta}^{\mathrm{base}} + \vec{\beta}^{\mathrm{BU}} x^{\mathrm{stim}} + \vec{\beta}^{\mathrm{TD}} x^{\mathrm{mod}} + \vec{\beta}^{\mathrm{inter}} x^{\mathrm{stim}} x^{\mathrm{mod}} \right) + \beta^0_{\mathrm{SVM}} \\ &= \vec{\beta}_{SVM} \cdot \left(\vec{\beta}^{BU} + \vec{\beta}^{\mathrm{inter}} x^{\mathrm{mod}} \right) x^{\mathrm{stim}} + \vec{\beta}_{SVM} \cdot \vec{\beta}^{\mathrm{TD}} x^{\mathrm{mod}} + C \end{aligned} \tag{19}$$

where $C = \beta^0_{\mathrm{SVM}} + \vec{\beta}_{SVM} \cdot \vec{\beta}^{\mathrm{base}}$ is a constant. The positive correlation between $\vec{\beta}_{\mathrm{SVM}}$ and $\vec{\beta}^{\mathrm{BU}}$ verifies that the SVM score is indeed sensitive to the presence of stimulus. The top-down modulation improves detection mainly through its interaction with the bottom-up stimulus, as captured by the term $\vec{\beta}_{\mathrm{SVM}} \cdot \vec{\beta}^{\mathrm{inter}}$. Top-down modulation effectively increasing acting as a gain increase of the SVM sensitivity to bottom-up input (from $\vec{\beta}^{\mathrm{BU}}$ to $\vec{\beta}^{\mathrm{BU}} + \vec{\beta}^{\mathrm{inter}} x^{\mathrm{mod}}$). The negative term $\vec{\beta}_{SVM} \cdot \vec{\beta}^{TD}$ reduces the false alarm rate in the absence of stimulus ($x^{\mathrm{stim}} = 0$), such that top-down modulation improves performance on stimulus-absent trials, by suppressing the SVM score and increasing the separation of SVM scores between trials with and without stimulus (**Figures 6A,F**).

Sensitivity Analysis and Singular Value Decomposition

Perturbations to cellular and synaptic parameters were performed and their effect on multiple circuit and behavioral features were evaluated (**Figures 8, S7**). The 6 perturbed parameters were (i) background excitatory input to TC neurons ($\mathrm{Bg}^{\mathrm{TC}}_{\mathrm{E}}$), (ii) T-type calcium conductance in TC neurons ($g^{\mathrm{TC}}_{\mathrm{CaT}}$), (iii) background excitatory input to RE neurons ($\mathrm{Bg}^{\mathrm{RE}}_{\mathrm{E}}$), (iv) T-type calcium conductance in RE neurons ($g^{\mathrm{RE}}_{\mathrm{CaT}}$), and (v, vi) the synaptic connections between the two neurons ($g^{\mathrm{AMPA}}_{\mathrm{TC}\to\mathrm{RE}}$ and $g^{\mathrm{GABA}}_{\mathrm{RE}\to\mathrm{TC}}$). The 7 evaluated circuit and behavioral features were (i) TC firing rate (r_0), (ii) response gain (k), (iii) spindle probability (P), (iv) detection sensitivity (S^{det}), (v) discrimination sensitivity (S^{disc}), (vi) congruent discrimination sensitivity (S^{cong}), and (vii) incongruent discrimination sensitivity (S^{inco}) . In particular, the 6 perturbed parameters are varied by $\pm 10\%$, and the feature sensitivity is defined as the change in the feature over the change in parameters. For instance, a feature sensitivity of 1 means that a 1% parameter perturbation alters the feature by 1%.

Specifically, we analyzed the feature sensitivity in the space of evaluated features, i.e., each perturbation is characterized by a column vector consisting of 7 different feature sensitivities. Therefore, we can obtain the feature sensitivity matrix X of dimension 7×6 within which each column represents one kind of perturbation (**Figure 8B**).

Singular value decomposition (SVD) is then performed on the sensitivity matrix X to find its principal components. The SVD of X is the factorization of X into the product of three matrices:

$$X = U\Sigma V^{\mathrm{T}},$$

where U and V are 7×7 and 6×6 unitary matrices, respectively. Σ is a rectangular diagonal matrix with positive real entries (corresponding singular values, usually assuming $\sigma_1 \geq \sigma_2 \geq \cdots$). Then, with the knowledge of linear algebra, one has

$$X^{\mathrm{T}}X = \sum_{i=1}^{6} \sigma_i^2 \mathbf{v_i} \mathbf{v_i}^{\mathrm{T}},$$

where $\mathbf{v_i}$ is the ith column vector of V. Therefore, we define $\frac{\sigma_i^2}{\sum_i \sigma_i^2}$, which represents the relative amount of reconstruction error reduced by including component i, as the fraction of the power in the feature sensitivity matrix associated with component i. It can be seen clearly that SVD is essentially principal component analysis (PCA) without mean subtraction. The first principal component from PCA captures the dominant pattern of variation. By contrast, the first component of SVD captures the dominant pattern of perturbation effects across features: $\mathbf{u_1}\sigma_1\mathbf{v_1}^{\mathrm{T}}$ is the closest rank-1 approximation of X.

Software Availability

Spiking circuit simulations were performed using the Brian2 simulator (Stimberg et al., 2019). Upon publication, custom modeling and analysis codes written in Python will be made publicly available on Github (https://github.com/murraylab), and a Brian2 implementation of the spiking circuit model will be made publicly available via the ModelDB model database (https://senselab.med.yale.edu/modeldb/).

Supplementary Figures

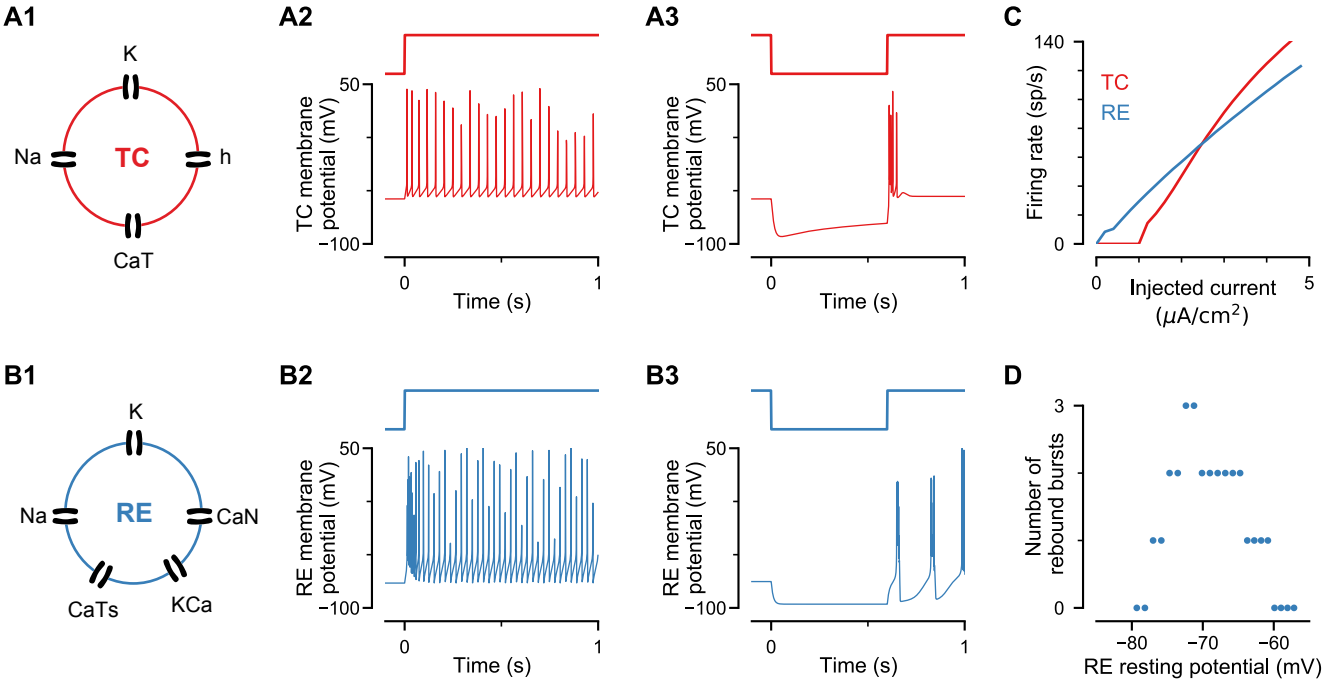

Figure S1: Single-compartment Hodgkin-Huxley Models of Thalamocortical (TC) and Reticular (RE) Neurons. **(A1)** The TC neuron model. Sodium (Na) and potassium (K) channels generate action potential spikes. Low-threshold calcium (CaT) and hyperpolarization-activated cation current (h) channels contribute to rebound spiking and bursting. **(A2)** Example TC membrane potential trace in response to depolarizing current input, exhibiting tonic spiking activity. **(A3)** Example TC membrane potential trace in response to hyperpolarization current input, exhibiting an initial sag due to h-current and a rebound burst of spiking following hyperpolarization offset. **(B1)** The thalamic reticular nucleus (RE) neuron model. Sodium (Na) and potassium (K) channels generate action potential spikes. Low-threshold calcium (CaT), calcium-activated potassium (KCa), and calcium-dependent nonspecific cation current (CaN) channels contribute to bursting. **(B2)** Example RE membrane potential trace in response to depolarizing current input, exhibiting tonic spiking activity. **(B3)** Example RE membrane potential trace in response to hyperpolarization current input, exhibiting multiple rebound bursts following hyperpolarization offset. textbf(C) Firing rate of TC (red) and RE (blue) model neurons as a function of constant injected current. **(D)** The number of rebound bursts of RE neurons as a function of resting potential. In this protocol, the RE neuron is first held, in steady state, at a resting potential which we control by different levels of injected current that is presented for the the entire trial. Then a second, hyperpolarizing injected current (-2.0 μA/cm^2) is applied for 500 ms. After cessation of this 500-ms hyperpolarizing injected current, the number of rebound bursts is recorded. The number of rebound bursts exhibited a bell-shaped dependence on the resting membrane potential. Similar dependence has been observed experimentally (Cueni et al., 2008; Wells et al., 2016).

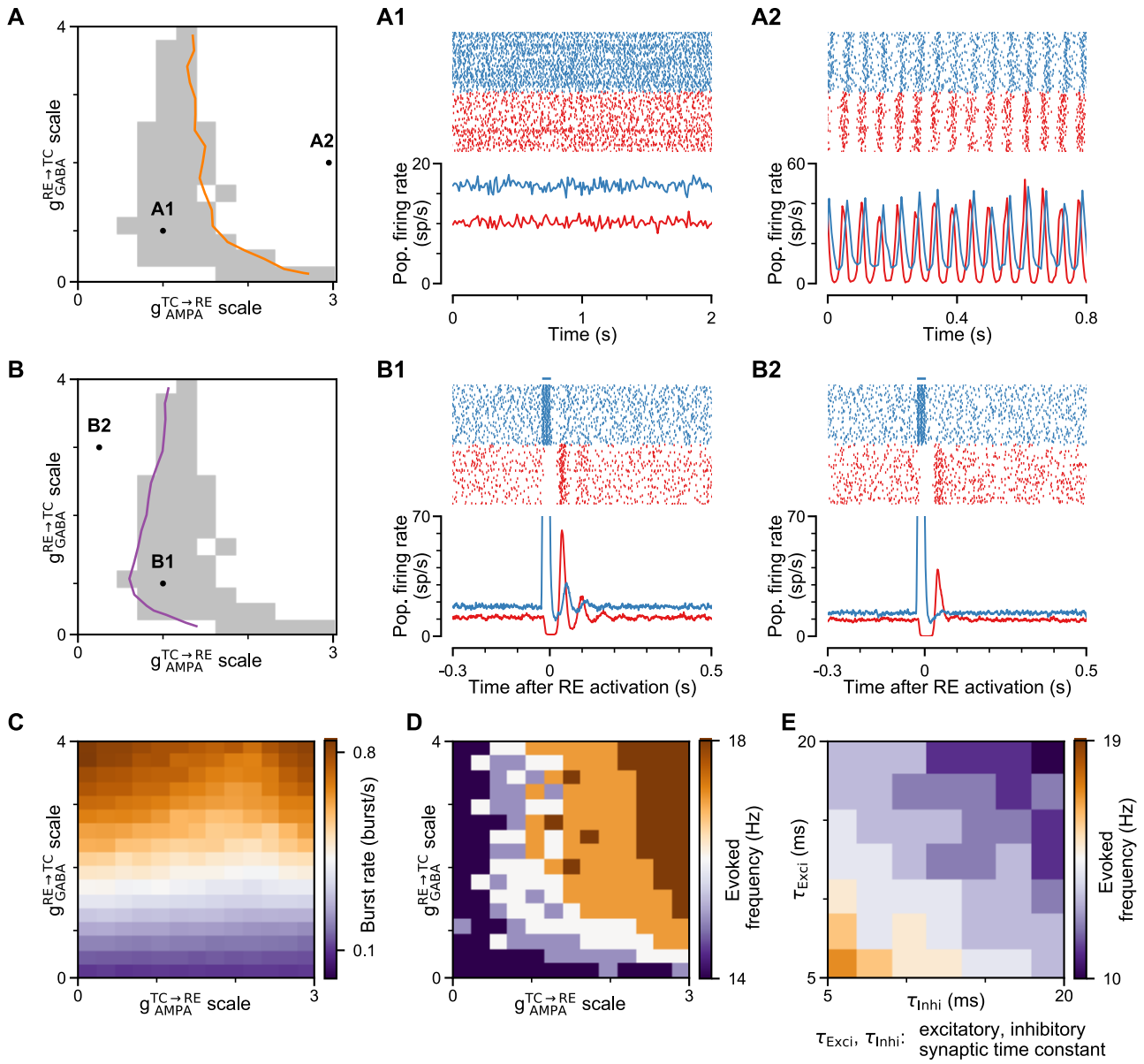

Figure S2: Dynamical Regimes of the TC-RE Circuit Model. (A) Spontaneous dynamics of circuit in two regimes of synaptic parameters (denoted by **A1** and **A2**). **(A1)** The circuit exhibits asynchronous spontaneous activity, consistent to the awake *in vivo* regime. **(A2)** Due to strong synaptic connectivity between TC and RE populations, the circuit model exhibits strong spontaneous synchronous oscillations. **(B)** Evoked response of circuit in two regimes of synaptic parameters (denoted by **B1** and **B2**). **(B1)** The circuit model demonstrates spindle-like transient oscillations in response to brief RE activation, consistent to the awake *in vivo* regime. **(B2)** The synaptic conductances of the circuit model are too weak to generate reverberating oscillations when perturbed. **(C)** Spontaneous burst rate of the circuit model with different synaptic parameters. **(D)** Evoked oscillation frequency of the circuit model with different synaptic parameters. **(E)** Evoked oscillation frequency of the circuit model with different synaptic time constants. Here, to preserve total synaptic strength, conductances are scaled inversely with the scaling of time constants. These results indicate that the intrinsic oscillation frequency in the circuit is shaped by both excitatory and inhibitory synaptic time constants.

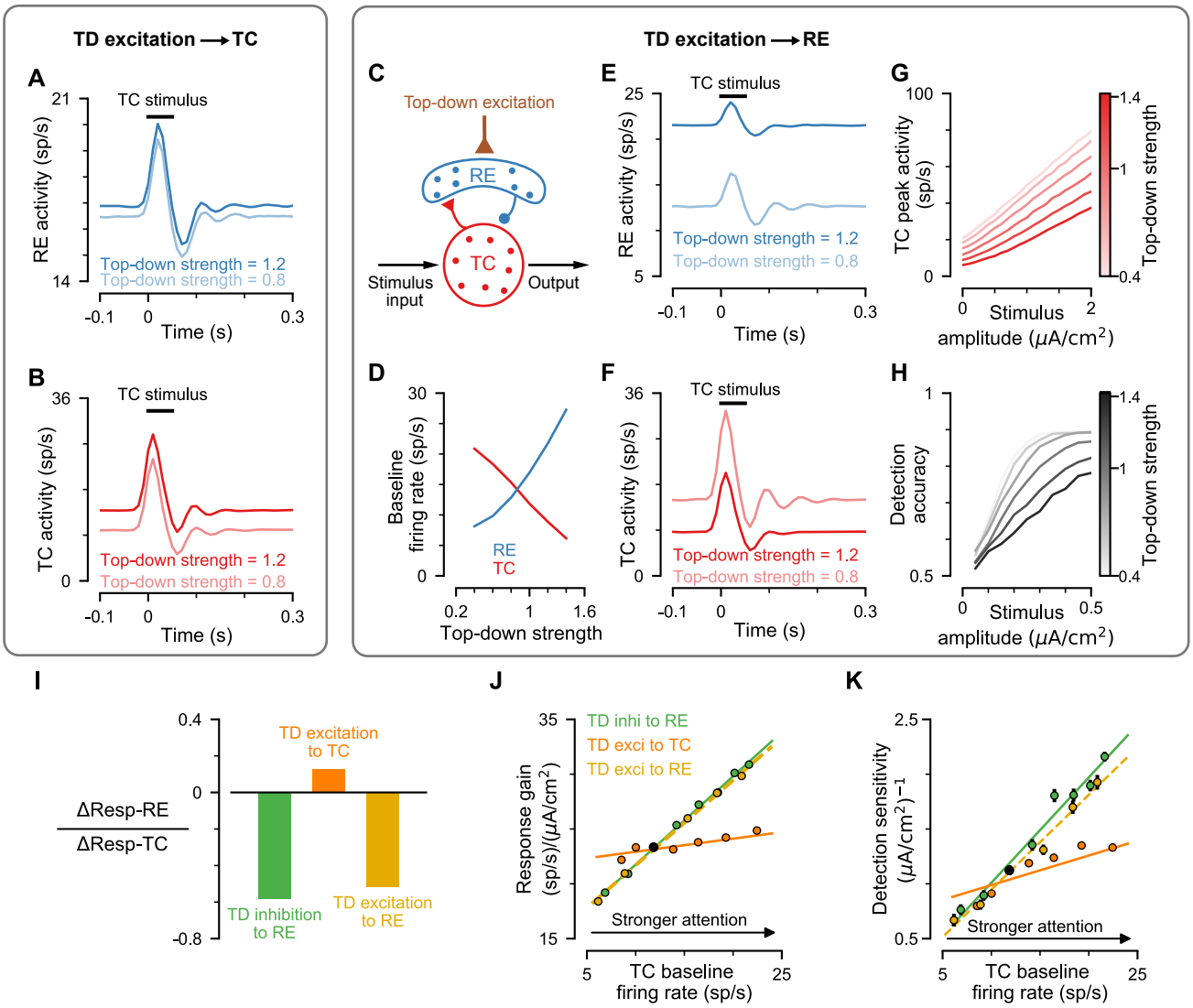

Figure S3: Top-down Excitation to TC or to RE. (A)-(B) RE and TC population activity in response to stimulus input with different strengths of top-down modulation (excitation) to TC. As shown in the experimental results, RE neurons also can receive excitatory modulatory inputs (Briggs and Usrey, 2008; Ahrens et al., 2015; Aizenberg et al., 2019). Thus, we also investigated the effect of top-down excitatory modulation through RE neurons shown in the following panels **C-H**. **(C)** Schematic of top-down excitation to RE neurons. **(D)** RE (blue) and TC (red) baseline firing rate as a function of top-down modulation strength (excitation to RE). Of note, the direction of modulation here is opposite of that for inhibition to RE **Figure 3**. **(E)** RE population activity in response to stimulus input with different top-down modulation strengths. Black bar denotes the time of TC stimulus onset. **(F)** TC Population activity in response to stimulus input with different top-down modulation strengths. Black bar denotes the time of TC stimulus onset. **(G)** Gain curves of TC sensory outputs under different levels of top-down modulation strength. Darker color represents stronger top-down strength. **(H)** Detection accuracy under different levels of top-down modulation strength. Darker color represents stronger top-down strength. **(I)** The ratio firing-rate changes for RE and TC neurons, for top-down modulation scenarios: inhibition to RE, excitation to TC, excitation to RE. The same change in TC firing rate can be obtained from the three different top-down modulations, but RE responses differentiate TD→TC from TD→RE scenarios. **(J)** Response gain of the circuit, as a function of top-down modulation strength, for the three scenarios. **(K)** Sensitivity of detection accuracy as a function of top-down modulation strength. Panels **(J)-(K)** show that top-down modulation via RE neurons has a stronger effect on response gain and detection performance, than via TC neurons. Black dots represent the control parameter set.

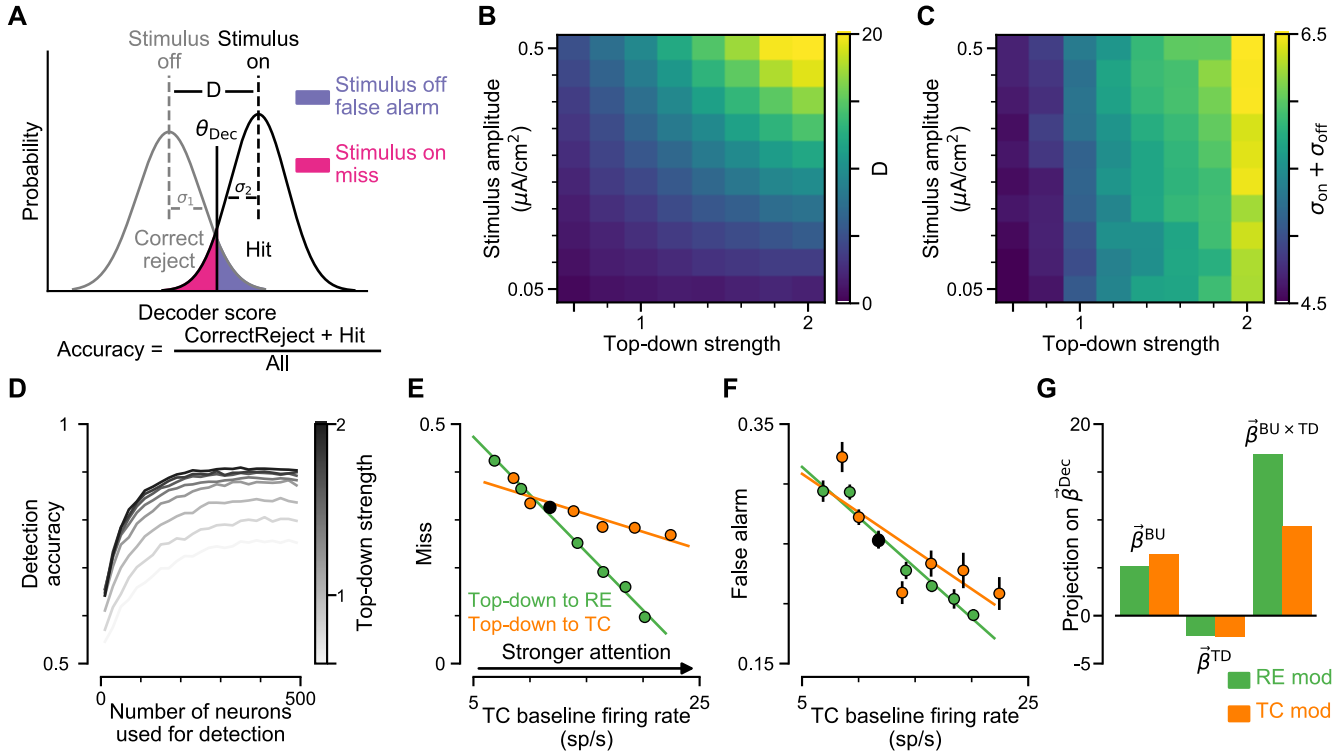

Figure S4: SVM decoder for detection and effects of top-down modulation via RE and TC neurons on decoding for detection. (A) Schematic of signal detection with the SVM decoder. Detection accuracy depends on the difference (D) between the mean of the SVM score distributions of stimulus present and absent, as well as, their standard deviations (σ_1, σ_2). **(B)** The mean difference between SVM score distributions of stimulus on and off as a function of bottom-up stimulus strength and top-down strength to RE. Both factors increase the score mean difference (D) with a strong impact. (C) The sum of standard deviations ($\sigma_{\text{on}} + \sigma_{\text{off}}$) as a function of bottom-up stimulus and top-down strength to RE. Both factors have small effect on the deviation (note range). These results indicate that stimulus and top-down inputs improve detection performance through their effects on the score difference D. **(D)** Detection accuracy as a function of the number of neurons used in the SVM decoder. **(E)** Proportion of stimulus-on trials which are misses, as a function of top-down modulation strength, with top-down modulation via either inhibition to RE neurons (green) or via excitation to TC neurons (orange). Here, TC baseline activity denotes a common proxy for the strength top-down modulation, to compare RE- and TC-mediated modulations. The rate of misses is reduced more effectively by RE modulation than by TC modulation. **(F)** Proportion of stimulus-off trials which are false alarms, as a function of top-down modulation strength, with top-down modulation via either inhibition to RE neurons (green) or via excitation to TC neurons (orange). Here, TC baseline activity denotes a common proxy for the strength top-down modulation, to compare RE- and TC-mediated modulations. The rate of false alarms is reduced similarly by both modulations. **(G)** Projections of the bottom-up stimulus, top-down modulation, and interaction weight vectors on the SVM vector weight. Top-down modulation via RE neurons (green) has a larger interaction term than top-down modulation via TC neurons, which is consistent with the results shown in **Figure 4** (i.e., RE modulation has a larger effect). The top-down modulation of baseline activity helps to reduce the false alarm rate, and top-down effect on output gain helps to reduce the miss rate.

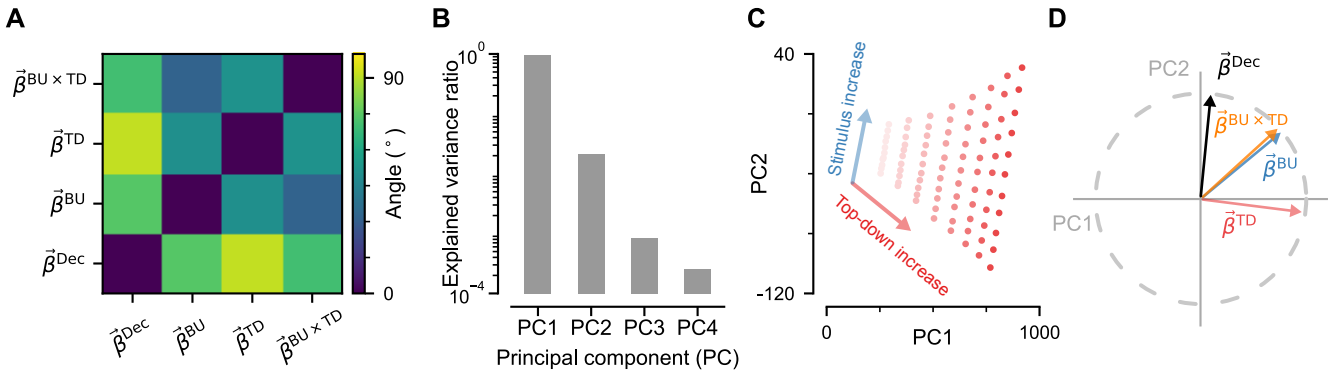

Figure S5: Geometric properties of circuit responses. (A) Angles between different vectors. The TD vector is nearly orthogonal to the decoder SVM vector (angle near 90°). BU and BU×TD are substantially aligned (indicated by a small angle). **B** Principal component analysis (PCA) of the firing rate response patterns under different stimulus amplitudes and top-down modulation strengths. PC1 and PC2 can explain 98.6% of the total variance. **C** Representation of circuit responses subspace of top PCs. The darker color represents the stronger top-down strength. The red and blue arrows indicate the increasing direction of top-down strength and stimulus amplitude, respectively. This visualization shows how increasing top-down strength enhances the separability of stimulus strengths, in relation to the dominant PCs. **D** The normalized bottom-up stimulus, top-down modulation, interaction, and decoder weight vectors within the PC1-PC2 subspace. The gray dashed circle is the unit circle. The TD vector is strongly aligned with PC1, and the the decoder weight vector is strongly aligned with PC2.

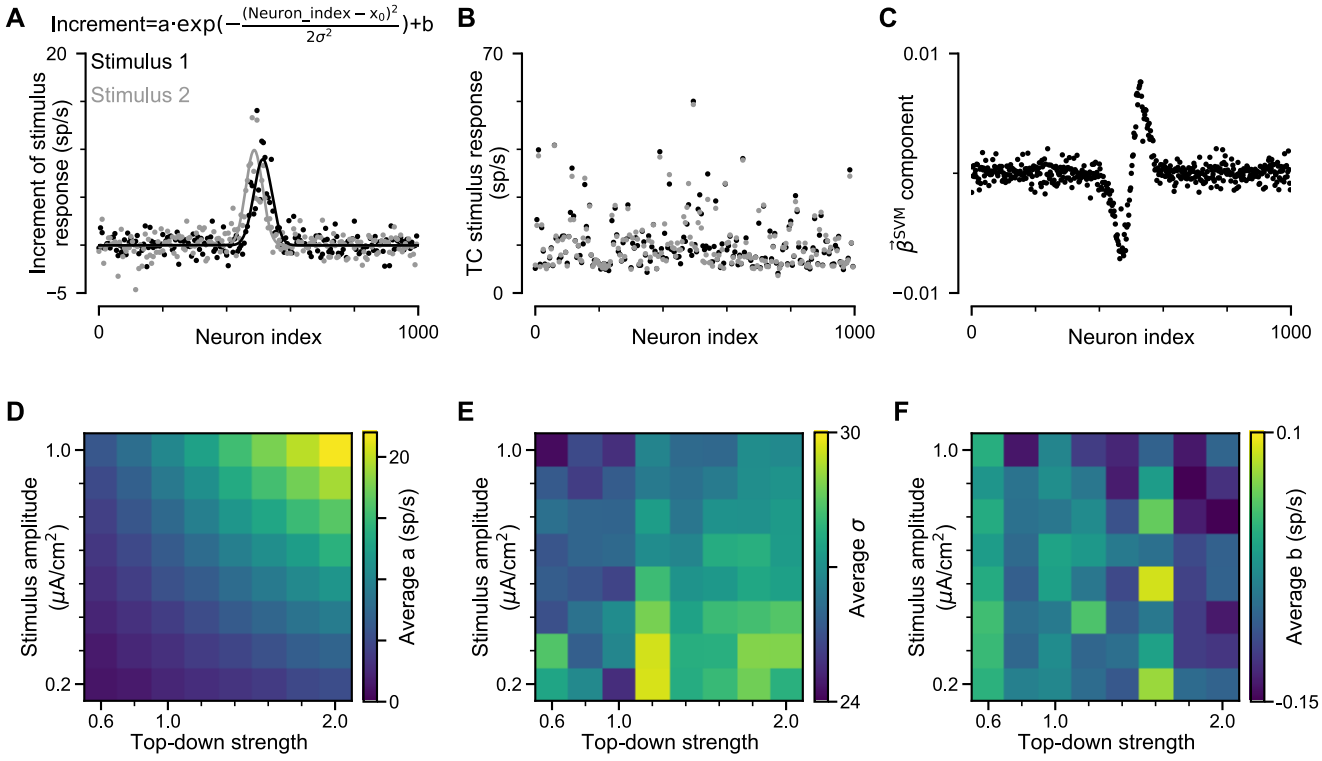

Figure S6: Analysis of SVM decoding for discrimination. (A) The TC firing rate with the tuned input as a function of the neuron index after subtracting the baseline firing rate. This shows the tuning and overlap of stimulus input patterns. The solid lines are fitted with top equations (Gaussian profile). **(B)** The TC firing rate as a function of the neuron index with the tuned input. The firing rate does not clearly show any tuned profile. **(C)**: The component profile of SVM weight vector as a function of the neuron index. It shows that there are distinct peaks at the centers of the tuned Stimulus 1 (positive) and Stimulus 2 (negative). **(D)-(F)** show the amplitude (a), the width (σ), and the baseline (b) of the firing rate profile under Stimulus 1 of different strength and top-down modulation. The strength of the input and top-down modulation heavily affects the amplitude of firing rate profile, while affect little of other factors. The value of each parameter is averaged by values from the two inputs.

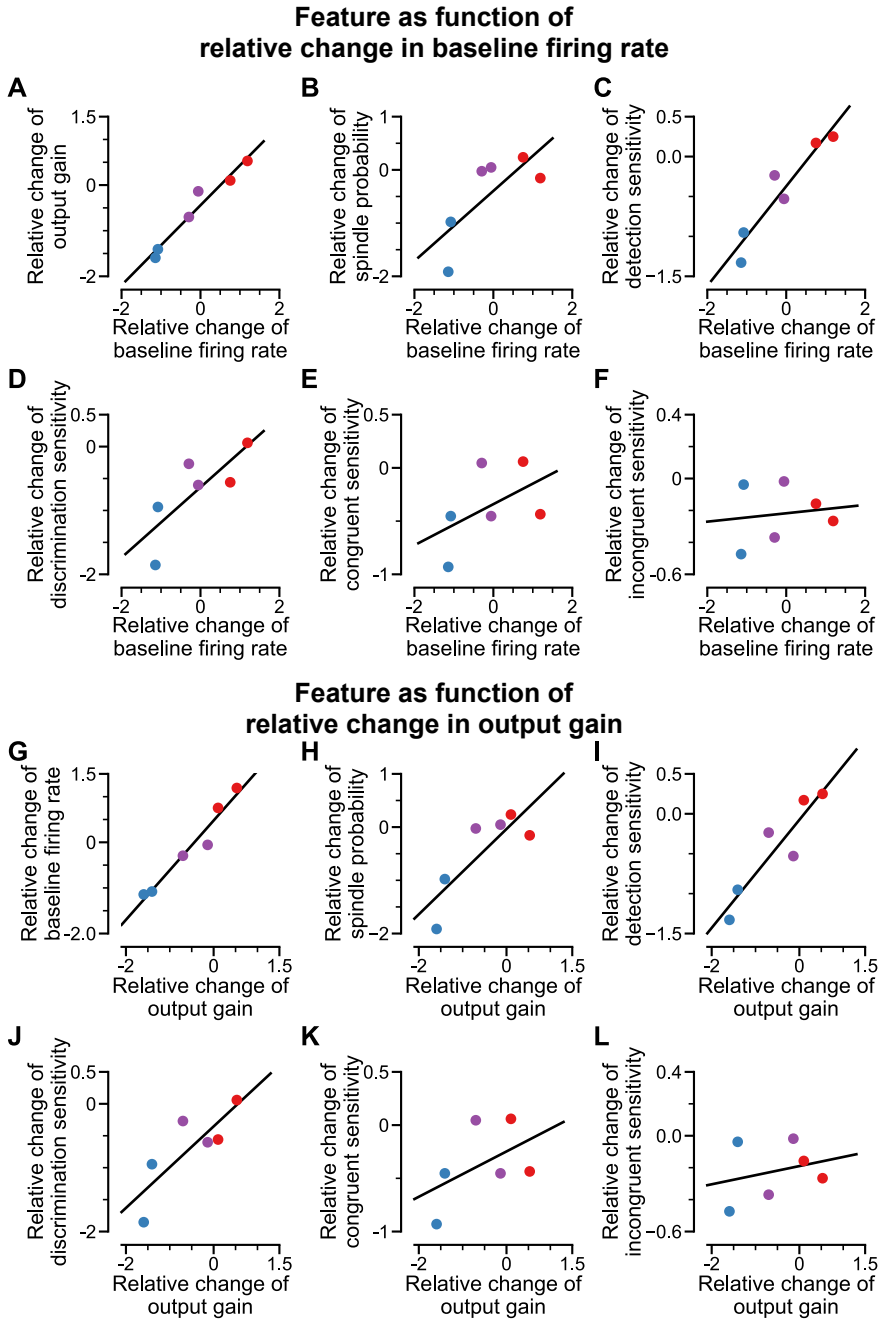

Figure S7: Dependences of circuit and behavioral features on perturbations. (A)-(F) Various circuit and behavioral measures as a function of varying TC baseline firing rate. **(G)-(L)**: Same as **(A)-(F)** but as a function of varying output gain.

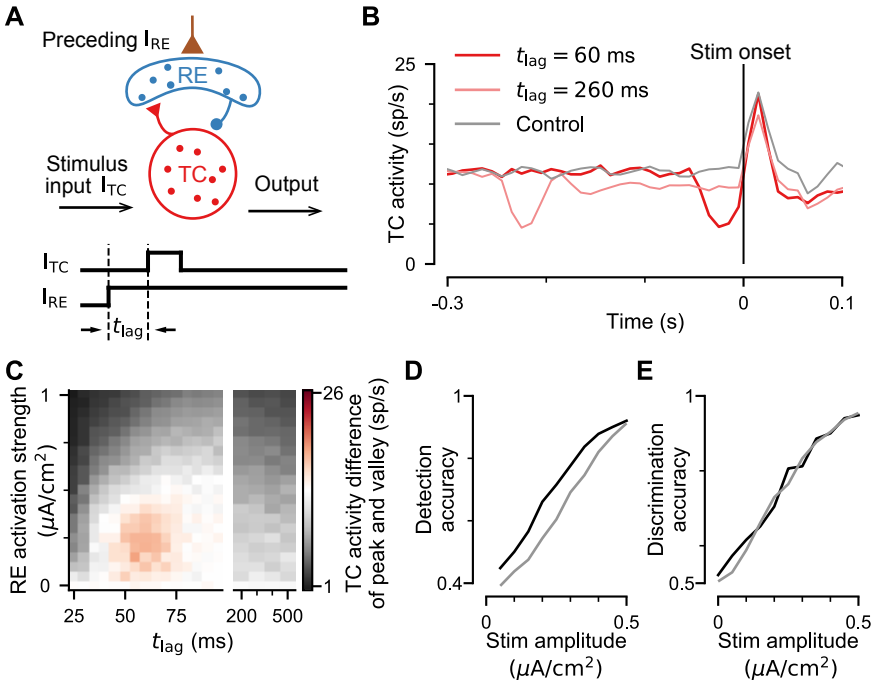

Figure S8: Effects of attention across time. **(A)** Schematic of paradigm, motivated by the experimental study of Aizenberg et al. (2019). A step increase in tonic top-down excitation ($\mathrm{I_{RE}}$) to RE precedes, by a time lag t_{lag}, a pulsed stimulus input to TC ($\mathrm{I_{TC}}$). **(B)** Evoked response to pulsed stimulus input to TC. When $t_{\mathrm{lag}} = 60$ ms, preceding excitation to RE suppresses TC spontaneous activity without affecting the peak evoked response of TC to the pulse input (solid dark red), relative to control without RE activation (dashed). However, the peak evoked response of TC is reduced in the case of $t_{\mathrm{lag}} = 260$ ms (light red). In this amplification scenario, excited RE neurons hyperpolarize TC neurons, activate its T-type Ca^{2+} channel, and resulted in the synchronous burst activity. These dynamics may related to experimental findings that thalamic burst spiking activity can facilitate the transmission of information to the cortex (Whitmire et al., 2016; Alitto et al., 2019). **(C)** TC response (i.e., the difference between maximum and minimum activity) as a function of RE activation strength and the time lag between RE and TC input onset. There is an enhancement for moderate RE activation strengths that is preferential for t_{lag} of approximately 50–70 ms. **(D)** Detection accuracy, from a linear SVM decoder, with (solid) or without (dashed) preceding RE activation, for $t_{\mathrm{lag}} = 60$ ms. Preceding RE activation substantially improves detection accuracy. **(E)** Discrimination accuracy, from a linear SVM decoder, with (solid) or without (dashed) preceding RE activation, for $t_{\mathrm{lag}} = 60$ ms. In contrast to detection, preceding RE activation does not have a substantial effect effect on discrimination accuracy.

References

Abbott L.F., and Chance F.S. (2005). Drivers and modulators from push-pull and balanced synaptic input. Prog Brain Res *149*, 147–55.

Ahrens S., Jaramillo S., Yu K., Ghosh S., Hwang G.R., Paik R., Lai C., He M., Huang Z.J., and Li B. (2015). ErbB4 regulation of a thalamic reticular nucleus circuit for sensory selection. Nat Neurosci *18*, 104–11.

Aizenberg M., Rolón-Martínez S., Pham T., Rao W., Haas J.S., and Geffen M.N. (2019). Projection from the amygdala to the thalamic reticular nucleus amplifies cortical sound responses. Cell Reports *28*, 605–615.e4.

Alitto H., Rathbun D.L., Vandeleest J.J., Alexander P.C., and Usrey W.M. (2019). The augmentation of retinogeniculate communication during thalamic burst mode. The Journal of Neuroscience *39*, 5697–5710.

Bastos A.M., Briggs F., Alitto H.J., Mangun G.R., and Usrey W.M. (2014). Simultaneous recordings from the primary visual cortex and lateral geniculate nucleus reveal rhythmic interactions and a cortical source for gamma-band oscillations. Journal of Neuroscience *34*, 7639–7644.

Bazhenov M., Timofeev I., Steriade M., and Sejnowski T. (2000). Spiking-bursting activity in the thalamic reticular nucleus initiates sequences of spindle oscillations in thalamic networks. J Neurophysiol *84*, 1076–87.

Bazhenov M., Timofeev I., Steriade M., and Sejnowski T.J. (2002). Model of thalamocortical slow-wave sleep oscillations and transitions to activated states. The Journal of Neuroscience *22*, 8691–8704.

Béhuret S., Deleuze C., and Bal T. (2015). Corticothalamic synaptic noise as a mechanism for selective attention in thalamic neurons. Frontiers in Neural Circuits *9*.

Briggs F., and Usrey W.M. (2008). Emerging views of corticothalamic function. Curr Opin Neurobiol *18*, 403–7.

Bruno R.M. (2006). Cortex is driven by weak but synchronously active thalamocortical synapses. Science *312*, 1622–1627.

Clemente-Perez A., Makinson S.R., Higashikubo B., Brovarney S., Cho F.S., Urry A., Holden S.S., Wimer M., Dávid C., Fenno L.E., Acsády L., Deisseroth K., and Paz J.T. (2017). Distinct thalamic reticular cell types differentially modulate normal and pathological cortical rhythms. Cell Reports *19*, 2130–2142.

Cotillon-Williams N., Huetz C., Hennevin E., and Edeline J.M. (2008). Tonotopic control of auditory thalamus frequency tuning by reticular thalamic neurons. J Neurophysiol *99*, 1137–51.

Crandall S.R., Cruikshank S.J., and Connors B.W. (2015). A corticothalamic switch: controlling the thalamus with dynamic synapses. Neuron *86*, 768–82.

Crick F. (1984). Function of the thalamic reticular complex: the searchlight hypothesis. Proc Natl Acad Sci U S A *81*, 4586–90.

Cueni L., Canepari M., Luján R., Emmenegger Y., Watanabe M., Bond C.T., Franken P., Adelman J.P., and Lüthi A. (2008). T-type Ca^{2+} channels, SK2 channels and SERCAs gate sleep-related oscillations in thalamic dendrites. Nat Neurosci *11*, 683–92.

Destexhe A., Babloyantz A., and Sejnowski T.J. (1993a). Ionic mechanisms for intrinsic slow oscillations in thalamic relay neurons. Biophys J *65*, 1538–52.

Destexhe A., Bal T., McCormick D.A., and Sejnowski T.J. (1996). Ionic mechanisms underlying synchronized oscillations and propagating waves in a model of ferret thalamic slices. J Neurophysiol *76*, 2049–70.

Destexhe A., Contreras D., Sejnowski T.J., and Steriade M. (1994). A model of spindle rhythmicity in the isolated thalamic reticular nucleus. J Neurophysiol *72*, 803–18.

Destexhe A., Contreras D., and Steriade M. (1998). Mechanisms underlying the synchronizing action of corticothalamic feedback through inhibition of thalamic relay cells. J Neurophysiol *79*, 999–1016.

Destexhe A., McCormick D.A., and Sejnowski T.J. (1993b). A model for 8-10 Hz spindling in interconnected thalamic relay and reticularis neurons. Biophys J *65*, 2473–7.

Fagerberg L., Hallström B.M., Oksvold P., Kampf C., Djureinovic D., Odeberg J., Habuka M., Tahmasebpoor S., Danielsson A., Edlund K., Asplund A., Sjöstedt E., Lundberg E., Szigyarto C.A.K., Skogs M., Takanen J.O., Berling H., Tegel H., Mulder J., Nilsson P., Schwenk J.M., Lindskog C., Danielsson F., Mardinoglu A., Sivertsson A., von Feilitzen K., Forsberg M., Zwahlen M., Olsson I., Navani S., Huss M., Nielsen J., Ponten F., and Uhlén M. (2014). Analysis of the human tissue-specific expression by genome-wide integration of transcriptomics and antibody-based proteomics. Mol Cell Proteomics *13*, 397–406.

Ferguson K.A., and Cardin J.A. (2020). Mechanisms underlying gain modulation in the cortex. Nature Reviews Neuroscience *21*, 80–92.

Fu Y., Tucciarone J.M., Espinosa J.S., Sheng N., Darcy D.P., Nicoll R.A., Huang Z.J., and Stryker M.P. (2014). A cortical circuit for gain control by behavioral state. Cell *156*, 1139–1152.

Golomb D., Wang X.J., and Rinzel J. (1996). Propagation of spindle waves in a thalamic slice model. J Neurophysiol *75*, 750–69.

Halassa M.M., and Acsády L. (2016). Thalamic inhibition: Diverse sources, diverse scales. Trends Neurosci *39*, 680–693.

Halassa M.M., and Kastner S. (2017). Thalamic functions in distributed cognitive control. Nat Neurosci *20*, 1669–1679.

Halassa M.M., Siegle J.H., Ritt J.T., Ting J.T., Feng G., and Moore C.I. (2011). Selective optical drive of thalamic reticular nucleus generates thalamic bursts and cortical spindles. Nat Neurosci *14*, 1118–20.

Hirai D., Nakamura K.C., ichi Shibata K., Tanaka T., Hioki H., Kaneko T., and Furuta T. (2017). Shaping somatosensory responses in awake rats: cortical modulation of thalamic neurons. Brain Structure and Function *223*, 851–872.

Hirsch J.A., Wang X., Sommer F.T., and Martinez L.M. (2015). How inhibitory circuits in the thalamus serve vision. Annu Rev Neurosci *38*, 309–29.

Hou G., Smith A.G., and Zhang Z.W. (2016). Lack of intrinsic gabaergic connections in the thalamic reticular nucleus of the mouse. J Neurosci *36*, 7246–52.

Huguenard J.R., and McCormick D.A. (2007). Thalamic synchrony and dynamic regulation of global forebrain oscillations. Trends in Neurosciences *30*, 350–356.

Jaramillo J., Mejias J.F., and Wang X.J. (2019). Engagement of pulvino-cortical feedforward and feedback pathways in cognitive computations. Neuron *101*, 321–336.e9.

Jones E.G. (2012). The thalamus (Springer Science & Business Media).

Kepecs A., and Fishell G. (2014). Interneuron cell types are fit to function. Nature *505*, 318–26.

Krauzlis R.J., Bogadhi A.R., Herman J.P., and Bollimunta A. (2018). Selective attention without a neocortex. Cortex *102*, 161–175.

Krishnan G.P., Chauvette S., Shamie I., Soltani S., Timofeev I., Cash S.S., Halgren E., and Bazhenov M. (2016). Cellular and neurochemical basis of sleep stages in the thalamocortical network. eLife *5*.

Krol A., Wimmer R.D., Halassa M.M., and Feng G. (2018). Thalamic reticular dysfunction as a circuit endophenotype in neurodevelopmental disorders. Neuron *98*, 282–295.

Li Y., Lopez-Huerta V.G., Adiconis X., Levandowski K., Choi S., Simmons S.K., Arias-Garcia M.A., Guo B., Yao A.Y., Blosser T.R., Wimmer R.D., Aida T., Atamian A., Naik T., Sun X., Bi D., Malhotra D., Hession C.C., Shema R., Gomes M., Li T., Hwang E., Krol A., Kowalczyk M., Peça J., Pan G., Halassa M.M., Levin J.Z., Fu Z., and Feng G. (2020). Distinct subnetworks of the thalamic reticular nucleus. Nature *583*, 819–824.

Litwin-Kumar A., Rosenbaum R., and Doiron B. (2016). Inhibitory stabilization and visual coding in cortical circuits with multiple interneuron subtypes. Journal of Neurophysiology *115*, 1399–1409.

Ly C., and Doiron B. (2009). Divisive gain modulation with dynamic stimuli in integrate-and-fire neurons. PLoS Computational Biology *5*, e1000365.

Martinez-Garcia R.I., Voelcker B., Zaltsman J.B., Patrick S.L., Stevens T.R., Connors B.W., and Cruikshank S.J. (2020). Two dynamically distinct circuits drive inhibition in the sensory thalamus. Nature *583*, 813–818.

McAlonan K., Cavanaugh J., and Wurtz R.H. (2008). Guarding the gateway to cortex with attention in visual thalamus. Nature *456*, 391–4.

Mehaffey W.H. (2005). Deterministic multiplicative gain control with active dendrites. Journal of Neuroscience *25*, 9968–9977.

Murray J.D., Jaramillo J., and Wang X.J. (2017). Working memory and decision-making in a frontoparietal circuit model. J Neurosci *37*, 12167–12186.

Nakajima M., and Halassa M.M. (2017). Thalamic control of functional cortical connectivity. Curr Opin Neurobiol *44*, 127–131.

Nakajima M., Schmitt L.I., and Halassa M.M. (2019). Prefrontal cortex regulates sensory filtering through a basal ganglia-to-thalamus pathway. Neuron *103*, 445–458.e10.

O'Connor D.H., Fukui M.M., Pinsk M.A., and Kastner S. (2002). Attention modulates responses in the human lateral geniculate nucleus. Nat Neurosci *5*, 1203–9.

Ozeki H., Finn I.M., Schaffer E.S., Miller K.D., and Ferster D. (2009). Inhibitory stabilization of the cortical network underlies visual surround suppression. Neuron *62*, 578–92.

Phillips J.W., Schulmann A., Hara E., Winnubst J., Liu C., Valakh V., Wang L., Shields B.C., Korff W., Chandrashekar J., Lemire A.L., Mensh B., Dudman J.T., Nelson S.B., and Hantman A.W. (2019). A repeated molecular architecture across thalamic pathways. Nat Neurosci *22*, 1925–1935.

Pinault D. (2004). The thalamic reticular nucleus: structure, function and concept. Brain Res Brain Res Rev *46*, 1–31.

Ramcharan E.J., Gnadt J.W., and Sherman S.M. (2005). Higher-order thalamic relays burst more than first-order relays. Proc Natl Acad Sci U S A *102*, 12236–41.

Rikhye R.V., Wimmer R.D., and Halassa M.M. (2018). Toward an integrative theory of thalamic function. Annu Rev Neurosci *41*, 163–183.

Ritter-Makinson S., Clemente-Perez A., Higashikubo B., Cho F.S., Holden S.S., Bennett E., Chkhaidze A., Rooda O.H.E., Cornet M.C., Hoebeek F.E., Yamakawa K., Cilio M.R., Delord B., and Paz J.T. (2019). Augmented reticular thalamic bursting and seizures in Scn1a-Dravet Syndrome. Cell Reports *26*, 54–64.e6.

Roberts J.A., and Robinson P.A. (2012). Corticothalamic dynamics: structure of parameter space, spectra, instabilities, and reduced model. Phys Rev E Stat Nonlin Soft Matter Phys *85*, 011910.

Rodenkirch C., Liu Y., Schriver B.J., and Wang Q. (2019). Locus coeruleus activation enhances thalamic feature selectivity via norepinephrine regulation of intrathalamic circuit dynamics. Nat Neurosci *22*, 120–133.

Saalmann Y.B., and Kastner S. (2011). Cognitive and perceptual functions of the visual thalamus. Neuron *71*, 209–223.

Saleem A.B., Lien A.D., Krumin M., Haider B., Rosón M.R., Ayaz A., Reinhold K., Busse L., Carandini M., and Harris K.D. (2017). Subcortical source and modulation of the narrowband gamma oscillation in mouse visual cortex. Neuron *93*, 315–322.

Sanzeni A., Akitake B., Goldbach H.C., Leedy C.E., Brunel N., and Histed M.H. (2020). Inhibition stabilization is a widespread property of cortical networks. eLife *9*.

Schmitt L.I., Wimmer R.D., Nakajima M., Happ M., Mofakham S., and Halassa M.M. (2017). Thalamic amplification of cortical connectivity sustains attentional control. Nature *545*, 219–223.

Sherman S.M. (2012). Thalamocortical interactions. Current Opinion in Neurobiology *22*, 575–579.

Sherman S.M. (2016). Thalamus plays a central role in ongoing cortical functioning. Nature neuroscience *19*, 533–541.

Sohal V.S., Pangratz-Fuehrer S., Rudolph U., and Huguenard J.R. (2006). Intrinsic and synaptic dynamics interact to generate emergent patterns of rhythmic bursting in thalamocortical neurons. J Neurosci *26*, 4247–55.

Soto-Sánchez C., Wang X., Vaingankar V., Sommer F.T., and Hirsch J.A. (2017). Spatial scale of receptive fields in the visual sector of the cat thalamic reticular nucleus. Nat Commun *8*, 800.

Stimberg M., Brette R., and Goodman D.F. (2019). Brian 2, an intuitive and efficient neural simulator. Elife *8*.

Temereanca S., Brown E.N., and Simons D.J. (2008). Rapid changes in thalamic firing synchrony during repetitive whisker stimulation. Journal of Neuroscience *28*, 11153–11164.

Timofeev I., Bonjean M.E., and Bazhenov M. (2020). Cellular Mechanisms of Thalamocortical Oscillations in the Sleeping Brain (New York, NY: Springer New York), pp. 119–170.

Usrey W.M., Reppas J.B., and Reid R.C. (1998). Paired-spike interactions and synaptic efficacy of retinal inputs to the thalamus. Nature *395*, 384–7.

Vantomme G., Rovó Z., Cardis R., Béard E., Katsioudi G., Guadagno A., Perrenoud V., Fernandez L.M.J., and Lüthi A. (2020). A thalamic reticular circuit for head direction cell tuning and spatial navigation. Cell Rep *31*, 107747.

Wang X.J., and Buzsáki G. (1996). Gamma oscillation by synaptic inhibition in a hippocampal interneuronal network model. J Neurosci *16*, 6402–13.

Wang X.J., Golomb D., and Rinzel J. (1995). Emergent spindle oscillations and intermittent burst firing in a thalamic model: specific neuronal mechanisms. Proc Natl Acad Sci U S A *92*, 5577–81.

Wei H., Bonjean M., Petry H.M., Sejnowski T.J., and Bickford M.E. (2011). Thalamic burst firing propensity: a comparison of the dorsal lateral geniculate and pulvinar nuclei in the tree shrew. J Neurosci *31*, 17287–99.

Wells M.F., Wimmer R.D., Schmitt L.I., Feng G., and Halassa M.M. (2016). Thalamic reticular impairment underlies attention deficit in Ptchd1$^{Y/-}$ mice. Nature *532*, 58–63.

Whitmire C.J., Waiblinger C., Schwarz C., and Stanley G.B. (2016). Information coding through adaptive gating of synchronized thalamic bursting. Cell Reports *14*, 795–807.

Wimmer R.D., Schmitt L.I., Davidson T.J., Nakajima M., Deisseroth K., and Halassa M.M. (2015). Thalamic control of sensory selection in divided attention. Nature *526*, 705–9.

Wolfart J., Debay D., Masson G.L., Destexhe A., and Bal T. (2005). Synaptic background activity controls spike transfer from thalamus to cortex. Nature Neuroscience *8*, 1760–1767.

Wong K.F., and Wang X.J. (2006). A recurrent network mechanism of time integration in perceptual decisions. J Neurosci *26*, 1314–28.

Yang G.R., Murray J.D., and Wang X.J. (2016). A dendritic disinhibitory circuit mechanism for pathway-specific gating. Nat Commun *7*, 12815.